Supporting information for: Understanding and suppressing non-radiative losses in methylammonium-free wide bandgap perovskite solar cells

Robert D. J. Oliver[#,a], Pietro Caprioglio[#,*,a], Francisco Peña-Camargo[b], Leonardo R. V. Buizza[a], Fengshuo Zu[c,d], Alexandra J. Ramadan[a], Silvia G. Motti[a], Suhas Mahesh[a], Melissa M. McCarthy[a], Jonathan H. Warby[b], Yen-Hung Lin[a], Norbert Koch[c,d], Steve Albrecht[e], Laura M. Herz[a], Michael B. Johnston[a], Dieter Neher[b], Martin Stolterfoht[b], Henry J. Snaith[*,a]

# These authors contributed equally

*corresponding authors: Pietro.caprioglio@physics.ox.ac.uk; henry.snaith@physics.ox.ac.uk

[a]Clarendon Laboratory, Department of Physics, Parks Road, Oxford, OX1 3PU

[b]Institute of Physics and Astronomy, University of Potsdam, Karl-Liebknecht-Str. 24-25, D-14476 Potsdam-Golm, Germany

[c]Helmholtz-Zentrum Berlin für Materialien und Energie GmbH, 12489 Berlin, Germany

[d]Institut für Physik & IRIS Adlershof, Humboldt-Universitat zu Berlin, 12489 Berlin, Germany

[e]Young Investigator Group Perovskite Tandem Solar Cells, Helmholtz-Zentrum Berlin für Materialien und Energie GmbH, Kekuléstraße 5, 12489 Berlin, Germany

Table of Contents

Experimental methods 3
Materials 3
Device fabrication 4
Photoluminescence measurements 5
Photovoltaic device characterisation 6
Terahertz Spectroscopy 8
Drift-diffusion simulations 10
Further Characterisation 12
Literature Search 13
Supporting data and discussion 15
Bulk Spectroscopic characterization 15
Modelling of the fluence-dependent TCSPC transients 17
Interface recombination 23
Fluence-dependent TCSPC on partial device stacks 24
Justification of double exponential fit 26
Photovoltaic device performance 28
Investigation of short-circuit current density increase 28
Recombination studies in devices 30

Experimental methods

Materials

Unless otherwise stated, all solvents used in work were purchased from Sigma Aldrich. All materials were used as received without additional purification. In this work, the perovskite thin films were processed at both the University of Potsdam and the University of Oxford. Any differences between the two processes are detailed below.

Substrates: Devices were fabricated in Potsdam with pre-patterned 25 mm x 25 mm indium tin oxide (ITO) substrates were purchased from Lumtec. The time-correlated single photon counting and THz spectroscopy measurements were performed on z-cut quartz substrates (area 1.3 cm^2).

Ionic additive: The ionic additive 1-butyl-1-methylpiperidinium tetrafluoroborate ($[BMP]^+[BF_4]^-$, purity 99 %) was purchased from Sigma Aldrich. The ionic additive was dissolved in a 4:1 volume ratio of dimethylformamide (DMF) and dimethylsulfoxide (DMSO) and shaken overnight.

Perovskite precursor: The $FA_{0.83}Cs_{0.17}Pb(I_{0.6}Br_{0.4})_3$ perovskite precursor solution was obtained by stoichiometrically weighing formamidinium iodide (FAI, GreatCell Solar), cesium iodide (CsI, AlfaAesar), lead iodide (PbI_2, TCI) and lead bromide ($PbBr_2$, AlfaAesar) in ambient air before being transferred into an N_2 filled glovebox. In Oxford, the materials were instead weighed in an N_2 filled glovebox. The precursor salts were dissolved in a mixture (4:1 ratio by volume) of dimethylformamide (DMF) and dimethylsulfoxide (DMSO). The precursors solution was shaken at room temperature overnight. To mix the ionic additive into the precursor solution, an appropriate volume of the ionic additive solution was added to the perovskite precursor solution to obtain a perovskite concentration of 1.3 M for the precursor and 0.5 $mgmL^{-1}$ of the ionic additive. For control devices, the same volume of neat DMF:DMSO was added to the perovskite precursor to achieve a concentration of 1.3 M. Both the control and ionic additive-containing precursor solutions were shaken for at least 30 mins pre-deposition. Explicitly, this was achieved by performing the following. Firstly, the precursor salts were weighed to within 1 mg according to values presented in **Table S1**. To this solution, 2 mL of solvent (4:1 DMF:DMSO) was added to achieve a nominal concentration of 1.56 M. This solution was shaken overnight to ensure the precursors had fully dissolved. This solution was then decanted into separated vials, 1 mL in each. We note there was residual precursor solution left due to volume expansion whilst the precursors dissolved. To one vial, 0.2 mL of neat DMF:DMSO was added to achieve a target concentration of 1.3 M. To the other 0.2 mL of ionic additive solution (3 $mgmL^{-1}$) was added to achieve a nominal 1.3 M perovskite containing 0.5 mg/mL of ionic additive.

Table S1: The masses of the precursor salts required to achieve a solution of a nominal concentration of 1.56 M when adding 2 mL of solvent (4:1 DMF:DMSO).

Precursor	**Mass (mg)**
FAI	445.3
CsI	137.8
PbI_2	575.3
$PbBr_2$	687.0

Transport layers: For the hole transport layer (HTL), poly(triaryl)amine (PTAA) was purchased from Sigma Aldrich and dissolved in toluene at a concretion of 1.75 mg/mL. For the surface modification layer, Poly(9,9-bis(3'-(N,N-dimethyl)-N-ethylammoinium-propyl-2,7-fluorene)-alt-2,7-(9,9-

dioctylfluorene))dibromide (PFN-Br) was purchased from TCI and dissolved at a concentration of 0.5 mg/mL in methanol. Buckminsterfullerene (C60) was purchased from Merck. Bathocuproine (BCP) was purchased from Sigma-Aldrich. LiF was purchased from Lumtec.

Device fabrication

Substrate preparation: The ITO substrates were cleaned by subsequent sonication in Hellmanex (3% in deionised water) acetone and isopropanol for 10 minutes in each solution. The substrates were then treated with UV-Ozone for 15 minutes before being transferred into an N_2 filled glovebox where the following deposition procedures took place.

HTL deposition: 70 uL of the PTAA solution was deposited onto a stationary substrate which accelerated to 6000 rpm over 3s where it remained for 30 s. Immediately after the program had finished, the substrate was annealed at 100 °C for 10 minutes. The substrates were allowed to return to room temperature following this procedure.

The PFN-Br layer was formed by dynamically depositing 60 uL of the PFN-Br solution onto the substrate spinning at 5000 rpm for 20 s. No anneal was performed following this step.

Perovskite layer deposition: For devices fabricated in Potsdam, 120 uL of perovskite precursor solution was deposited onto a static substrate. The substrate accelerated to 3500 rpm over 3s where it remained for 35s. After 10s, 200 uL of ethylacetate was dropped onto the substrate. At the end of the spincoating procedure, the films were annealed at 100 °C for 1 hour.

For samples made in Oxford on z-cut quartz substrates, 50 uL of the precursor solution was dynamically deposited onto the substrate spinning at 1000 rpm. After 5s, the spin speed increased to 5000 rpm over 5s, where it remained for 30s. An antisolvent quench was performed by depositing 50 uL of anisole onto the substrate 5s before the end of the program. The films were annealed for 30 minutes at 100 °C.

ETL deposition: After annealing, the samples were allowed to cool before being transferred to a custom evaporation chamber. C60 was deposited at 0.2 A/s to achieve a thickness of 30 nm. Following this deposition, 8 nm of bathocuproine at a rate of 0.1 A/s. All depositions took place under high vacuum (~10^{-7} mbar).

LiF deposition: If present, LiF was deposited at a rate of 0.2 A/s until a thinkness of 1 nm was achieved.

Metal electrode deposition: Copper was used as the top electrode for devices made in Potsdam. 100 nm of Cu was deposited under high vacuum (~10^{-7} mbar) at a rate of 0.3-0.7 A/s to achieve a thickness of 100 nm. The active area of the solar cells is 6 mm^2 and is defined by the overlap of the ITO and Cu electrodes.

Photoluminescence measurements

Photoluminescence quantum yield

Absolute photoluminescence measurements were performed as per our previous reports.[1–4] In brief, a continuous wave 520 nm laser diode (Insaneware) was coupled into an optical fibre which entered an integrating sphere to photoexcite the sample. The intensity of the laser was equivalent to the 1 sun AM1.5 illumination. To confirm this calibration, a solar cell of the appropriate bandgap was illuminated in the integrating sphere and its J_{sc} was measured to be in good agreement with the value determined from a solar simulator. The light from the sphere was coupled into a second optical fibre which was measured using an Andor SR393i-B spectrometer.

The integrating sphere and fibre were calibrated by shining a halogen lamp of known spectrum into the sphere. A spectral correction factor was determined to ensure the detected spectrum of the lamp matched its known spectral irradiance.

To determine the absolute photon number, the corrected spectral irradiance was first divided by the photon energy (to give spectral photon density) and then numerical integration was performed to obtain the absolute photon count for both excitation and photoluminescence. To verify the accuracy of these measurements, three test samples (purchased from Hamamatsu Photonics) of known PLQY (~70 %) were measured. We determined the PLQY of the test samples to within a small (< 5%) relative error.

Intensity dependent photoluminescence measurements

To adjust the excitation intensity, the laser was first attenuated using a variable neutral density filter. The intensity was determined by a separate Si photodiode. The PL measurements were then performed in the integrating sphere as described above.

Quasi-Fermi Level Splitting (QFLS) determination

The quasi-Fermi level splitting (QFLS) was determined in-line with our previous work.[1] In brief, we calculate the QFLS according to

$$QFLS = k_{\mathrm{B}}T \ln\left(PLQY \frac{J_{\mathrm{G}}}{J_{0,\mathrm{rad}}}\right),$$

where k_{B} is the Boltzmann constant, T the absolute temperature, PLQY the photoluminescence quantum yield, J_{G} is the generation current and $J_{0,\mathrm{rad}}$ is the radiative recombination current in the dark. The generation current can be calculated according to

$$J_{\mathrm{G}} = q \int_0^{\infty} \mathrm{d}\lambda \, EQE(\lambda) \varphi_{\mathrm{AM1.5}}(\lambda)$$

where q is the elementary charge, EQE is the photovoltaic external quantum efficiency and $\varphi_{\mathrm{AM1.5}}$ is the solar photon flux. In a similar manner, one calculates $J_{0,\mathrm{rad}}$ as

$$J_{0,\mathrm{rad}} = q \int_0^{\infty} \mathrm{d}\lambda \, EQE(\lambda) \varphi_{\mathrm{BB}}(\lambda)$$

with φ_{BB} being the blackbody spectrum at room temperature.

Steady-State Photoluminescence Measurements

Photoluminescence (PL) spectra were measured following excitation by a 398 nm continuous wave laser (PicoHarp, LDH-D-C-405M) at a power density of 290 mWcm^{-2}. The emitted PL was collected and coupled into a grating spectrometer (Princeton Instruments SP-2558), after which light was detected by an iCCD camera (PI-MAX4, Princeton Instruments). Measurements were carried out under vacuum (< 1×10^{-3} mbar).

Time-Resolved Photoluminescence Measurements

Time-Correlated Single Photon Counting was carried out using the same laser as above to photoexcite the thin films, but in pulsed excitation mode with a repetition rate of 1 MHz for isolated films, and 2.5 MHz for those with transport layers attached. Photoluminescence was collected using the same monochromator, with a photon-counting detector (PDM series from MPD). Timing is controlled electronically using a PicoHarp300 event timer. PL decays were measured at the peak wavelengths of the PL spectra. Measurements were carried out under vacuum (< 1×10^{-3} mbar).

Time-Resolved Photoluminescence Fitting

For the isolated films, a least-squares fit was carried out on the lowest-fluence PL decays using a stretched exponential of the form $I = I_0 e^{-\left(\frac{t}{\tau_{char}}\right)^{\beta}}$.[5] The average decay lifetime was then calculated as $\tau_{av} = \left(\frac{\tau_{char}}{\beta}\right)\Gamma\left(\frac{1}{\beta}\right)$, and the monomolecular recombination rate was obtained as $k_1 = \frac{1}{2\tau_{av}}$.[6]

For the films with transport layers attached, a least squares fit was carried out at each fluence using a double exponential $I = A_1 e^{-t/T1} + A_2 e^{-t/T2}$. This was necessary to account for the two separate processes that result in the PL transient, namely charge transfer into the transport layer and (interfacial) recombination. This fitting also ensures a smooth numerical derivative, which is important for the calculation of the differential lifetime.

Photovoltaic device characterisation

Current density – voltage characteristics

For devices measured in Potsdam, current density – voltage curves were obtained in a 2-wire source-sense configuration with a Keithley 2400. The samples were illuminated using an Oriel class AAA Xenon lamp-based sun simulator at an intensity of approximately 100 mW cm^{-2} of AM1.5G irradiation. The illumination intensity was monitored simultaneously with a Si photodiode. The exact illumination intensity was used for efficiency calculations, and the simulator was calibrated with a KG5 filtered silicon solar cell (certified by Fraunhofer ISE). The obtained short-circuit current density is checked by integrating the product of the External Quantum Efficiency and the solar spectrum which matches the obtained J_{SC} within less than 3%. The temperature of the cell was fixed to 25 °C and a voltage ramp (scan rate) of 0.2 V/s was used.

Intensity dependent open-circuit voltage measurements

Intensity dependent V_{OC} measurements were performed using a continuous wave laser of central wavelength 445 nm (Insaneware). A continuously variable neutral density filterwheel (ThorLabs) was used to attenuate the laser power (up to OD 6).

The light intensity was simultaneously measured with a silicon photodetector and a Keithley 485 to ensure the accuracy of the measurement. The measurement was performed by first measuring the open-circuit voltage at a given intensity and a variable exposure time to ensure steady-state was achieved. Then the device was taken to short circuit for 1 second whilst the filter wheel rotated to the next position. A custom-built Labview program was written to automate the measurement. To check whether the V_{oc} reached steady-state conditions, the temporal evolution of the open-circuit voltage and the J_{sc} was recorded with a resolution of 200 ms. Moreover, the exposure time was varied before the V_{oc} value was taken at each intensity step which did not lead to significant changes in the open-circuit voltage as previously reported. [2]

Pseudo-JV determination

The *pJV* curves were determined as follows, in line with our recent publication.[2] Firstly, illumination intensity-dependent PLQY or V_{OC} measurements were performed. The PLQY measurements were converted into QFLS values as described above. Then the intensity axis was converted to current density, by setting the current density value at 1-sun to be 95 % of the radiative potential (in this case ~19.0 mAcm^{-2}). The axes were then inverted so the horizontal axis was voltage (from V_{OC} or QFLS/q measurements) and the vertical axis a current. Then, we subtract each value of the current by the generation current which ensures 0 V corresponds to J_{SC} conditions and 0 mAcm^{-2} to the open-circuit voltage equivalent.

External quantum efficiency (EQE)

The external quantum efficiency of our devices was determined using Fourier transform photocurrent spectroscopy. Our custom-built set up is based on a Bruker Vertex 80v Fourier transform interferometer. The solar cells were masked with a metal aperture such that the whole active area was illuminated by a tungsten halogen lamp. To determine the EQE, the photocurrent spectrum of the device under test was divided by that of a calibrated Si reference cell (Newport) of a known EQE. The acquisition time for each photocurrent spectrum was approximately 60 seconds.

To determine the short-circuit current from the EQE measurements, the overlap integral of the AM1.5 photon flux ($\varphi_{\mathrm{AM1.5}}$) with the EQE was calculated. Explicitly, this is given by

$$J_{\mathrm{sc}} = q \int_0^{\infty} \mathrm{d}\lambda \, EQE(\lambda) \varphi_{\mathrm{AM1.5}}(\lambda)$$

where q is the elementary charge and λ is the wavelength.

Terahertz Spectroscopy

Optical-Pump Terahertz-Probe Spectroscopy

An amplified laser system (Spectra Physics, MaiTai - Empower - Spitfire) with a central wavelength 800 nm, 35 fs pulse duration and 5 kHz repetition rate was used to generate THz radiation via the inverse spin hall effect[7] and was detected using free-space electro-optic sampling with a 1 mm-thick ZnTe (110) crystal, a Wollaston prism and a pair of balanced photodiodes. The THz pulse was measured in transmission geometry. The pump beam was frequency-doubled to 400nm by a β-barium- borate (BBO) crystal.

OPTP Fitting

We follow the same process outlined by Wehrenfennig et al.[8] Recombination in metal-halide perovskites can generally be well-described by the following differential equation [9]:

$$\frac{\partial n}{\partial t} = -k_1 n - k_2 n^2 - k_3 n^3 \qquad S1$$

Here k_1 is the monomolecular trap-mediated (or Shockley-Read-Hall) recombination rate constant, k_2 is the bimolecular radiative recombination rate constant, and k_3 is the trimolecular Auger recombination rate constant.

The change in transmitted THz radiation $\frac{\Delta T}{T}(t) \equiv x(t)$ is proportional to the photoexcited charge-carrier density in the thin film:

$$n(t) = \phi\, C\, x(t) \qquad S2$$

Here ϕ indicates the number of free charge-carriers generated per photon, and $C = \tilde{n}_0 \,/\, x(0)$ is the proportionality factor between the initial THz response $x(0)$ and the absorbed photon density $\tilde{n}_0$, given by:

$$\tilde{n}_0 = \frac{E\, \lambda\, \alpha(\lambda)}{h\, c\, A_{eff}} \left(1 - R_{pump}(\lambda)\right) \qquad S3$$

The effective overlap area A_{eff} can be calculated from the pump and probe beam parameters, whilst the absorption and reflection coefficients are measured for each sample. Although for very high excitation fluences (> 50 μJcm^{-2}) the proportionality in equation S2 no longer holds, the fluences employed here were all below this threshold (at most 34 μJcm^{-2}), meaning that we calculate C as the average value across all fluences.

Substituting equation S2 into S1 gives us:

$$\begin{aligned} \frac{\mathrm{d}x}{\mathrm{d}t} &= -C^2 \phi^2 k_3 x^3 - C\phi k_2 x^2 - k_1 x \\ &= -A_3 x^3 - A_2 x^2 - A_1 x \end{aligned} \qquad S4$$

In this case, given that fluences were kept below 34 μJcm^{-2} (equivalent to a photoexcited charge-carrier density of $n \approx 5 \times 10^{18}$ cm^{-3}), Auger recombination was found to contribute negligibly. Thus, setting $A_3 = 0$, an analytical solution can be found to the ODE:

$$x(t) = \frac{A_1 \alpha}{e^{A_1 t} - \alpha A_2} \quad \text{for} \quad \frac{1}{\alpha} = \frac{A_1}{x(0)} + A_2, \qquad S5$$

These solutions are fitted globally to the decays across all fluences in order to extract the rate constants A_i. The value of k_1, and thus A_1, is fixed using the value obtained from TCSPC measurements, as detailed above. The values of k_2 is then calculated as $k_2 = \frac{A_2}{\phi C}$ (assuming $\phi = 1$ i.e. that all photons are converted to free charges, as is typical in most bulk 3D perovskites[10]).

Finally, in order to account for an initial spatially varying charge-carrier density (due to absorption following the Beer-Lambert law), the fitting algorithm takes into account an exponentially decaying charge-carrier density. This is done by dividing the sample into 30 equally thick slices and computing the decay function for each of these individually.

Calculation of Charge-Carrier Mobilities and Diffusion Lengths

Charge-carrier mobility is linked to the photoconductivity of a thin film by:

$$\mu = \frac{\Delta S \, A_{eff}}{Ne} \qquad S6$$

Here ΔS is the sheet conductivity of the film, A_{eff} is the effective overlap area of the optical pump and THz probe beams, *N* is the number of photoexcited free charge carriers, and *e* is the elementary charge.

Given that THz wavelengths are both much longer than the perovskite film thickness ($\lambda_{THz} \gg d_{film}$), and shorter than the quartz substrate thickness ($\lambda_{THz} < d_{substrate}$), we can use the following approximation for the sheet photoconductivity of a thin film between two media with refractive indeces n_A and n_B:

$$\Delta S = -\epsilon_0 c (n_A + n_B) \left(\frac{\Delta T}{T}\right) \qquad S7$$

Here $\Delta T = T_{excited} - T_{dark}$ is the photoinduced change in THz electric field, and $n_A = 1$ for vacuum and $n_B = 2.13$ for a z-cut quartz substrate.

We determine the number of photoexcited charge-carriers using:

$$N = \phi \frac{E \, \lambda}{h \, c} \Big(1 - R_{pump}(\lambda)\Big) \Big(1 - T_{pump}(\lambda)\Big), \qquad S8$$

where *E* is the energy contained in an optical excitation pulse of wavelength λ (= 400 nm), R_{pump} and T_{pump} are the sample reflectivity and tramittance at 400 nm, and ϕ is the branching ratio of photons-to-free-charges.

We can substitute equations S7 and S8 into S6, in order to obtain:

$$\phi\mu = -\epsilon_0 c(n_A + n_B)\frac{A_{eff}hc}{Ee\lambda\left(1 - R_{pump}(\lambda)\right)\left(1 - T_{pump}(\lambda)\right)}\left(\frac{\Delta \mathrm{T}}{\mathrm{T}}\right) \qquad S9$$

Given that the branching ratio $0 \leq \phi \leq 1$, the calculated effective charge-carrier mobility is always an underestimate; it is only identical to the true free-carrier mobility when there is full conversion of photons to free charges, although this is typically the case for bulk 3D perovskites[10]. Further, the determined charge-carrier mobility arises from contributions to the conductivity from both free electrons and free holes, and these cannot be separated. Thus, the effective mobility values shown in **Figure S3** are the sum of electron and hole mobilities.

Finally, the charge-carrier diffusion lengths were calculated as:

$$L_D = \left(\frac{\mu k_B T}{eR(n)}\right)^{\frac{1}{2}} = \left(\frac{\mu k_B T}{e(k_1 + nk_2)}\right)^{\frac{1}{2}} \qquad S10$$

For the values shown in **Figure S3**, a charge-carrier density of $n = 10^{15}\mathrm{cm}^{-3}$ was used to calculate the diffusion lengths, which is similar to the photo-generated density in metal-halide perovskite photovoltaic devices in normal operation under AM1.5 irradiation[9].

Drift-diffusion simulations

The simulations were performed using SCAPS (Solar Cell Capacitance Simulator), which is an open-source software package that can be obtained from https://users.elis.ugent.be/ELISgroups/solar/projects/scaps upon the conditions requested by the developers Marc Burgelman et al.[11] The simulation parameters used are detailed below in **Table S2**.

Table S2: SCAPs simulation parameters used for control and IA-modified devices.

Parameter (perovskite)	Value (Control)	Value (IA)	Comment
Band gap	1.8 eV	1.8 eV	From optical measurements presented in figure S1.
Electron affinity	3.8 eV	3.8 eV	This leads to band misalignments of 0.1 eV at each interface, consistent with the V_{OC}-QFLS mismatch we observe.[1]

Dielectric permittivity (relative)	22	22	
CB effective density of states	1.5×10^{18} cm^{-3}	1.5×10^{18} cm^{-3}	
VB effective density of states	1.5×10^{18} cm^{-3}	1.5×10^{18} cm^{-3}	
Electron thermal velocity	1×10^{7} cm/s	1×10^{7} cm/s	
Hole thermal velocity	1×10^{7} cm/s	1×10^{7} cm/s	
Electron mobility	1 $cm^2V^{-1}s^{-1}$	1 $cm^2V^{-1}s^{-1}$	The THz mobilities were higher than this, however, a better fit to the JVcurves shown in Figure 1 was obtained with a mobility of 1 cm^2 /Vs, which might be related to grain boundaries. This value is consistent with simulation values used in the literature.[12,13]
Hole mobility	1 $cm^2V^{-1}s^{-1}$	1 $cm^2V^{-1}s^{-1}$	
Shallow uniform donor density	1×10^{10} cm^{-3}	1×10^{10} cm^{-3}	
Shallow uniform acceptor density	1×10^{10} cm^{-3}	1×10^{10} cm^{-3}	
Radiative recombination coefficient	5×10^{-11} cm^3/s	5×10^{-11} cm^3/s	Measured using THz spectroscopy, figure 1a in the main text and Figure S3.
Parameter (perovskite defect)	**Value (Control)**	**Value (IA)**	**Comment**
Defect type	Neutral	Neutral	
Electron capture cross section	1×10^{-15} cm^2	1×10^{-15} cm^2	
Hole capture cross section	1×10^{-15} cm^2	1×10^{-15} cm^2	
Trap profile	Uniform	Uniform	
Trap density	2.2×10^{14} cm^{-3}	1.1×10^{14} cm^{-3}	These values set the bulk lifetimes to be 450 ns, and 900 ns as determined from our TCSPC on the bulk perovskite
Parameter (HTL)	**Value (Control)**	**Value (IA)**	**Comment**
Band gap	3.0 eV	3.0 eV	
Electron affinity	2.5 eV	2.5 eV	This leads to band misalignments of 0.1 eV at each interface, consistent with the V_{OC}-QFLS mismatch we observe.[1]
Dielectric permittivity (relative)	3.5	3.5	
CB effective density of states	1×10^{20} cm^{-3}	1×10^{20} cm^{-3}	
VB effective density of states	1×10^{20} cm^{-3}	1×10^{20} cm^{-3}	
Electron thermal velocity	1×10^{7} cm/s	1×10^{7} cm/s	
Hole thermal velocity	1×10^{7} cm/s	1×10^{7} cm/s	
Electron mobility	$1 \times 10^{-5}$$cm^2V^{-1}s^{-1}$	$1 \times 10^{-5}$$cm^2V^{-1}s^{-1}$	
Hole mobility	$1 \times 10^{-4}$$cm^2V^{-1}s^{-1}$	$1 \times 10^{-4}$$cm^2V^{-1}s^{-1}$	
Shallow uniform donor density	1×10^{5} cm^{-3}	1×10^{5} cm^{-3}	
Shallow uniform acceptor density	1×10^{5} cm^{-3}	1×10^{5} cm^{-3}	
Parameter (HTL defect)	**Value (Control)**	**Value (IA)**	**Comment**
Defect type	Neutral	Neutral	
Electron capture cross section	1×10^{-15} cm^2	1×10^{-15} cm^2	
Hole capture cross section	1×10^{-15} cm^2	1×10^{-15} cm^2	
Trap profile	Uniform	Uniform	
Trap density	1×10^{17} cm^{-3}	1×10^{17} cm^{-3}	

Parameter (HTL/perovskite interface)	Value (Control)	Value (IA)	Comment
Defect type	Acceptor	Acceptor	
Electron capture cross section	1 x 10^{-16} cm^2	1 x 10^{-16} cm^2	
Hole capture cross section	1 x 10^{-16} cm^2	1 x 10^{-16} cm^2	
Total density	1.3 x 10^{12} cm^{-2}	0.45 x 10^{12} cm^{-2}	This sets the SRV at each HTL interface to be those that were determined in Table 1 in the main text.
Parameter (ETL)	**Value (Control)**	**Value (IA)**	**Comment**
Band gap	2.0 eV	2.0 eV	
Electron affinity	3.9 eV	3.9 eV	
Dielectric permittivity (relative)	5.0	5.0	
CB effective density of states	1 x 10^{20} cm^{-3}	1 x 10^{20} cm^{-3}	
VB effective density of states	1 x 10^{20} cm^{-3}	1 x 10^{20} cm^{-3}	
Electron thermal velocity	1 x 10^{7} cm/s	1 x 10^{7} cm/s	
Hole thermal velocity	1 x 10^{7} cm/s	1 x 10^{7} cm/s	
Electron mobility	1 x $10^{-2}$$cm^2V^{-1}s^{-1}$	1 x $10^{-2}$$cm^2V^{-1}s^{-1}$	
Hole mobility	1 x $10^{-2}$$cm^2V^{-1}s^{-1}$	1 x $10^{-2}$$cm^2V^{-1}s^{-1}$	
Shallow uniform donor density	1 x 10^{5} cm^{-3}	1 x 10^{5} cm^{-3}	
Shallow uniform acceptor density	1 x 10^{5} cm^{-3}	1 x 10^{5} cm^{-3}	
Parameter (ETL defect)	**Value (Control)**	**Value (IA)**	**Comment**
Defect type	Neutral	Neutral	
Electron capture cross section	1 x 10^{-15} cm^2	1 x 10^{-15} cm^2	
Hole capture cross section	1 x 10^{-15} cm^2	1 x 10^{-15} cm^2	
Trap profile	Uniform	Uniform	
Trap density	1 x 10^{17} cm^{-3}	1 x 10^{17} cm^{-3}	
Parameter (HTL/perovskite interface)	**Value (Control)**	**Value (IA)**	**Comment**
Defect type	Donor	Donor	
Electron capture cross section	1 x 10^{-16} cm^2	1 x 10^{-16} cm^2	
Hole capture cross section	1 x 10^{-16} cm^2	1 x 10^{-16} cm^2	
Total density	5.6 x 10^{12} cm^{-2}	0.64 x 10^{12} cm^{-2}	This sets the SRV at each ETL interface to be those that were determined in Table 1 in the main text.

All other values used are consistent with SCAPS simulations presented in the literature.[12,13] In particular, ref 12 provides detailed information from each parameter is determined.

Further Characterisation

Ellipsometry

The optical constants were measured using a Woollam RC2 Ellipsometer. The ellipsometer was calibrated using a reference silicon wafer with 20 nm SiO2 on top. Ellipsometric data (Ψ–δ) was acquired at four angles:45°, 55°, 65°, 75°.The software CompleteEASE was used to model the data.

The data was first fitted to the Cauchy relation in a small region of the sub-bandgap region. A B-spline was used to fit the remainder of the spectrum. The extinction co-efficient was set to zero below the bandgap. Kramers-Kronig consistency was maintained.

Ultraviolet photoemission spectroscopy

UPS was conducted using a monochromated helium discharge lamp (HIS 13 FOCUS GmbH, photon energy of 21.22 eV) in an ultrahigh vacuum system (base pressure of 1×10^{-9} mbar). All spectra were recorded at room temperature and normal emission using a hemispherical electron analyser (SPECSPhoibos 100). Secondary electrons cut-off (SECO) spectra were conducted at a negative bias of 10 V. Thickness of the C60 layer was monitored using a quartz crystal microbalance, thus corresponding a mass-thickness.

All samples were transferred directly from the N_2-filled glove box into the vacuum chamber without exposing to ambient air.

UV-vis. Absorption

Absorption spectra were taken using a Bruker Vertex 80v Fourier-Transform Infrared (FTIR) spectrometer, with a tungsten halogen source and a silicon diode detector. Measurements were carried out under low vacuum (< 5 mbar).

X-ray diffraction data

X-ray diffraction patterns were measured using a Panalytical X'pert powder diffractometer with a copper Kα X-ray source, λ = 0.1541 nm.

Literature Search

Perovskite	Structure	Bandgap (eV)	V_{oc} (V)	PCE (%)	V_{oc}/V_{oc}^{SQ}	Reference
$Cs_{0.17}FA_{0.83}Pb(I_{0.75}Br_{0.25})_3$	p-i-n	1.68	1.10	15.4	0.79	[14]
$Cs_{0.25}FA_{0.75}Pb(I_{0.8}Br_{0.2})_3$	p-i-n	1.68	1.10	17.4	0.79	[14]
$Cs_{0.17}FA_{0.83}Pb(I_{0.6}Br_{0.4})_3$	p-i-n	1.75	1.13	14.3	0.77	[14]
$Cs_{0.4}FA_{0.6}Pb(I_{0.7}Br_{0.3})_3$	p-i-n	1.75	1.17	16.3	0.80	[14]
$FA_{0.6}Cs_{0.4}Pb(I_{0.7}Br_{0.3})_3$	p-i-n	1.76	1.14	14.6	0.77	[15]

$FA_{0.6}Cs_{0.3}DMA_{0.1}Pb(I_{0.8}Br_{0.2})_3$ DMA is dimethylammonium	p-i-n	1.71	1.20	19.2	0.84	[16]
$FA_{0.8}Cs_{0.2}Pb(I_{0.5}Br_{0.5})_3$	p-i-n	1.82	1.15	8.6	0.75	[17]
$FA_{0.8}Cs_{0.2}Pb(I_{0.5}Br_{0.5})_3$	p-i-n	1.82	1.18	11.4	0.77	[17]
$FA_{0.8}Cs_{0.2}Pb(I_{0.5}Br_{0.5})_3$	p-i-n	1.82	1.19	12.3	0.78	[17]
$FA_{0.83}Cs_{0.17}Pb(I_{0.9}Br_{0.1})_3$	p-i-n	1.6	1.07	17.6	0.81	[18]
$FA_{0.83}Cs_{0.17}Pb(I_{0.9}Br_{0.1})_3$ with ionic additive	p-i-n	1.6	1.12	20.3	0.85	[18]
$FA_{0.83}Cs_{0.17}Pb(I_{0.77}Br_{0.23})_3$	p-i-n	1.66	1.11	16.6	0.80	[18]
$FA_{0.83}Cs_{0.17}Pb(I_{0.77}Br_{0.23})_3$ with ionic additive	p-i-n	1.66	1.16	17.3	0.84	[18]
$FA_{0.8}Cs_{0.2}Pb(I_{0.6}Br_{0.4})_3$	p-i-n	1.77	1.16	15.0	0.78	[19]
$FA_{0.8}Cs_{0.2}Pb(I_{0.6}Br_{0.4})_3$ VNPB HTL	p-i-n	1.77	1.20	15.9	0.81	[19]

Supporting data and discussion

Bulk Spectroscopic characterization

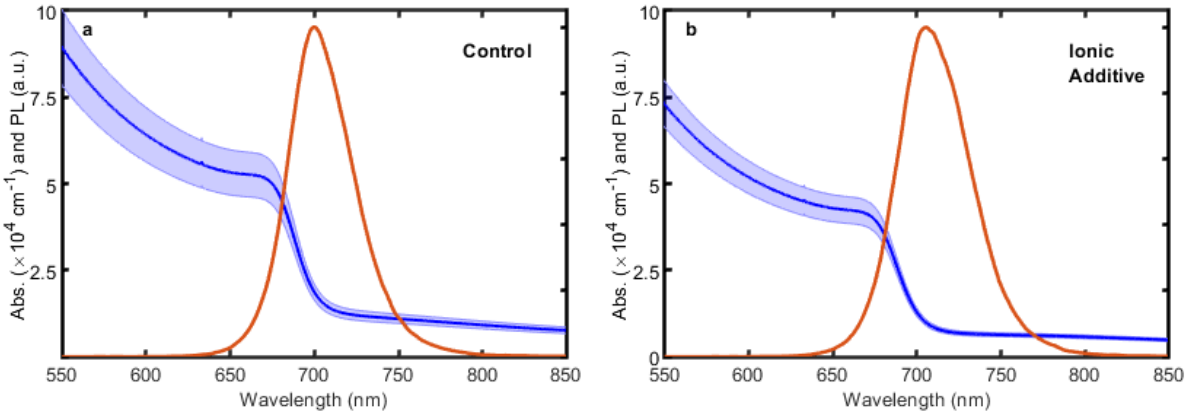

Figure S1: Absorption coefficient (blue, with shaded error) and normalized photoluminescence (orange) spectra for a) control and b) ionic additive modified thin films on quartz. The absorption spectra were measured using a Bruker Vertex 80v FTIR spectrometer, and the PL spectra were measured under CW excitation at 398 nm at a power density of 290 $mWcm^{-2}$. The samples show very similar absorption onsets at approximately 700 nm, with the PL spectra peaking at similar wavelengths with very low Stokes shifts.

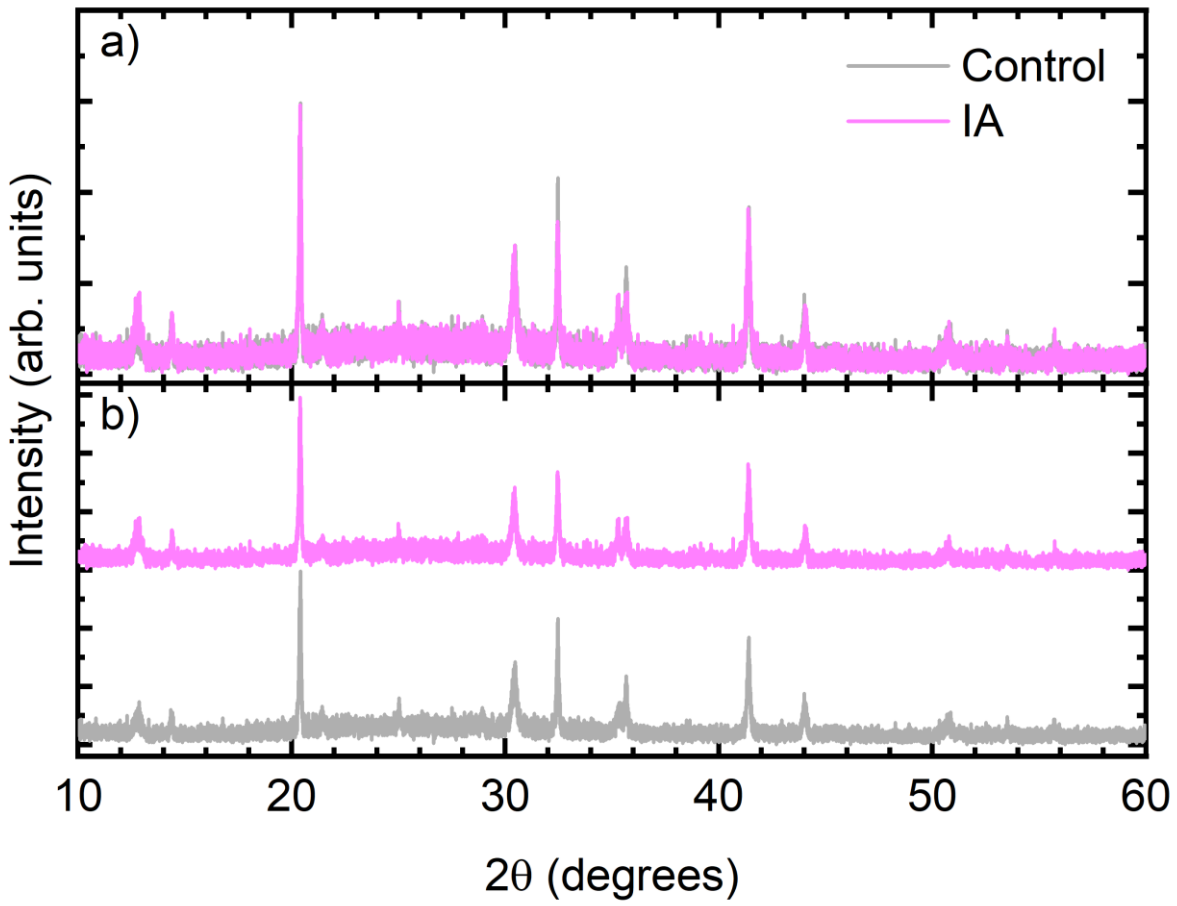

Figure S2: X-ray diffraction patterns for control (grey) and IA (pink) perovskite thin films on ITO substrates. Panel a) shows the patterns overlaid and panel b) shows the same data offset to allow for comparison. The incident X-ray wavelength was λ = 0.152 nm. The XRD patterns are almost identical in each case.

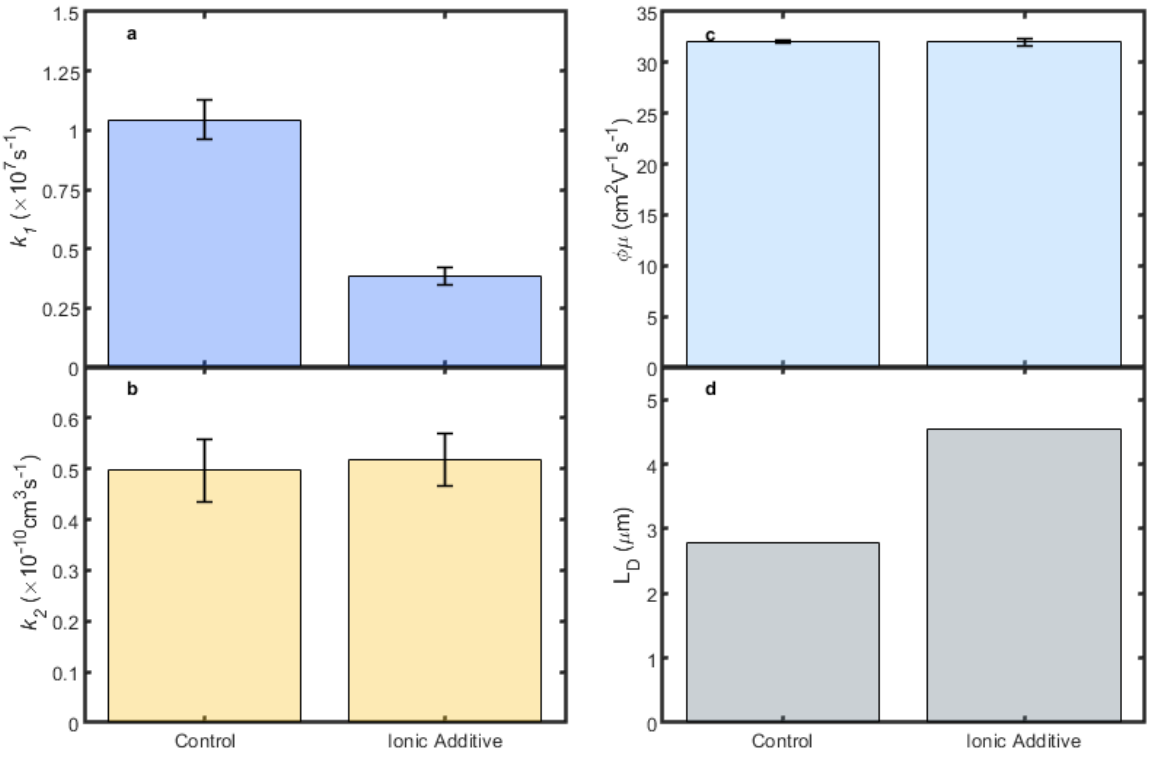

Figure S3: (a) Monomolecular recombination rate constants k_1 extracted from stretched exponential fits to time-resolved PL decays (see Experimental Methods above for details). (b) Bimolecular recombination rate constants k_2 obtained from fits to OPTP photoconductivity decays (see Experimental Methods above for details). (c) Charge-carrier mobility values measured using OPTP spectroscopy. Both compositions displayed remarkably good mobilities above 32 $cm^2V^{-1}s^{-1}$. (d) Charge-carrier diffusion lengths calculated from the measured charge-carrier recombination rate constants and mobilities. The larger diffusion length for the sample with ionic liquid additive is due to the lower monomolecular recombination rate constant for that sample.

Modelling of the fluence-dependent TCSPC transients

To better understand the impact of the ionic additives on the charge-carrier dynamics, we investigated the fluence dependence of the PL decays. As observed in **Figures 1c and 1d** in the main text, the PL decays recorded for the control sample are characterised by stretched dynamics and an enhanced shortening of lifetimes with increasing excitation fluence with respect to the ionic additive sample.

We first try to reproduce this behaviour with the same rate equation model used for the analysis of OPTP dynamics (see **equation S1**). Notably, the differences in the PL dynamics cannot be reproduced only by changes in the first order recombination rate constant k_1 (associated with trap-assisted recombination). **Figure S4** shows how the fluence dependence observed is only reproduced by substantially different bimolecular recombination rates (described by k_2). While the bimolecular radiative rate constant is intrinsic of the semiconductor and should remain unchanged upon trap

passivation, the observed effective value of k_2 can be affected by diffusion and reabsorption effects.[20] These effects, however, should be clearly visible in the OPTP dynamics, contrary to our observations in the present case, where the OPTP dynamics recorded from the control and ionic additive samples (**Figures 1a and 1b** in the main text) are very similar and can be fitted with essentially the same effective k_2.

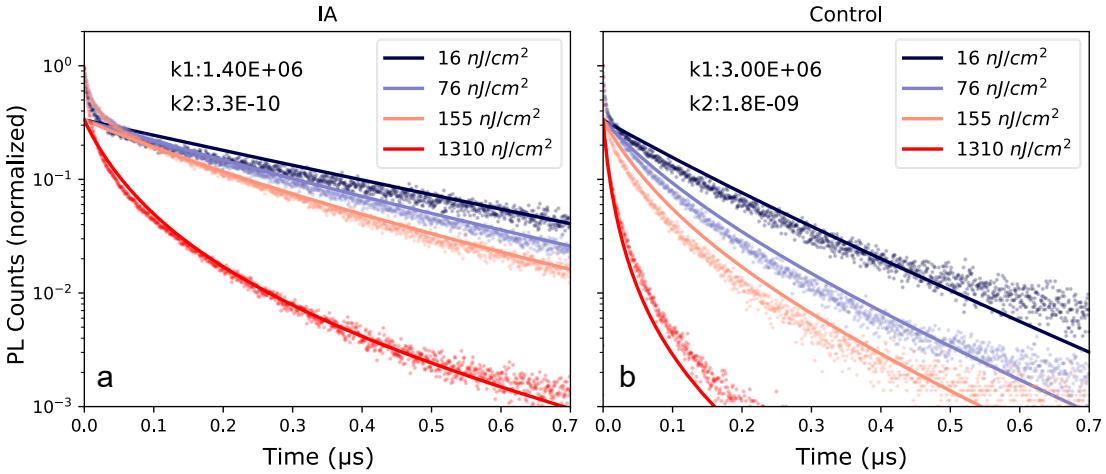

Figure S4. Experimental (dots) and modelled (lines) PL dynamics using a simple rate equation model as adopted for OPTP analysis and described in Equation S1; (a) The dynamics of the perovskite film with ionic additives can be well reproduced, with recombination rate constants that are in good agreement with the OPTP analysis and literature values[20,21] (b) The intensity dependence of dynamics observed in the control film, reproduced by significantly higher values for bimolecular radiative recombination rates (k_2). Early-time fast decay has been neglected in this case.

To explain the observed differences in PL dynamics we then need to consider the particular experimental factors that influence the PL and OPTP measurements. Firstly, the PL dynamics are recorded at lower excitation densities, and therefore experience more significant impact of trap states. And secondly, the PL is acquired with a higher repetition rate of the pulsed photoexcitation (1MHz, as opposed to 5kHz in the OPTP experiment). Given the long lifetimes of trapped carriers in these lead halide perovskite semiconductors,[22] the shorter time period between photoexcitation pulses can result in trap-filling and population build-up. The effect of the repetition rate on the photoexcited state dynamics depends on trapping and the balance of electron/hole lifetimes. To investigate the impact of higher repetition rate, we consider a model (similarly previously reported in ref. [23]) that describes the decay of electron and hole populations (n and p, respectively) as

$$\frac{dn}{dt} = -k_{tn}n - k_2np \qquad (S11)$$

$$\frac{dp}{dt} = -k_{tp}p - k_2np \qquad (S12)$$

where k_{tn} and k_{tp} are the first order decay rate constants for electrons and holes, respectively, and k_2 is the bimolecular radiative rate constant. Third order processes are not being incorporated here because of the relatively low charge-carrier densities in the experiments under consideration. The PL dynamics is then given by

$$PL = k_2 np \qquad (S13)$$

To account for charge-carrier build-up, the remaining populations at the time of arrival of the next pulse are used as initial conditions for the next iteration. The process is repeated for 50 pulses, when steady-state conditions are reached. The rates were adjusted to reproduce the fluence-dependent dynamics, and the value for k_2 was kept fixed for both samples (in agreement with the observation of unchanged higher order recombination in the OPTP dynamics).

The PL dynamics shows a sharp decay at early-time that is likely associated with surface effects and/or the diffusion of charge carriers away from the initial photogeneration profile.[4,24] According to the high charge-carrier mobilities in these semiconductors, diffusion is expected to result in a uniform distribution across the thickness of the film within a few nanoseconds. As a first step in the implementation of our model, we neglect the early-time dynamics and consider the initial condition to be a uniform distribution of charge-carriers across the thickness of the film.

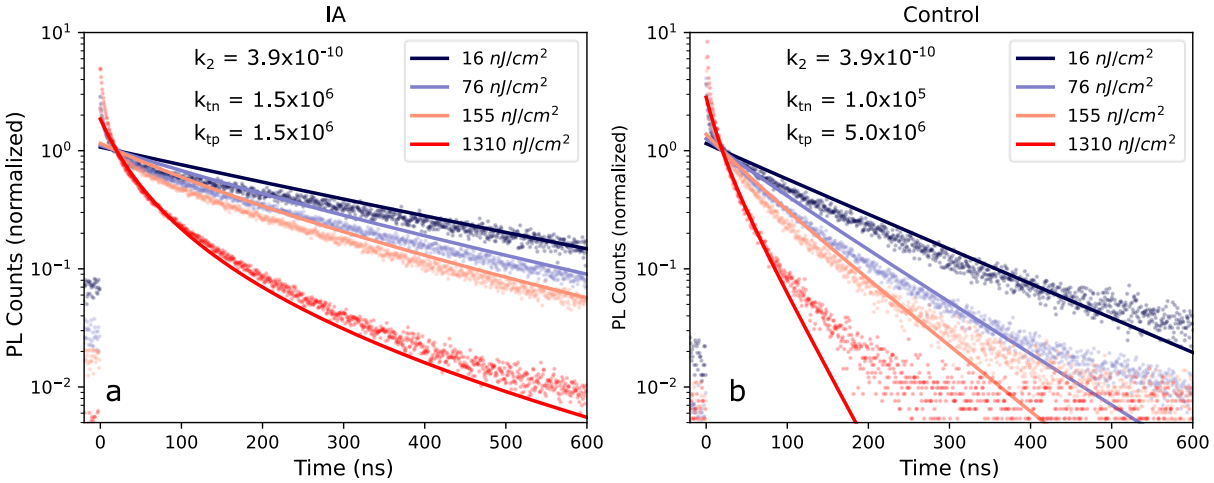

Figure S5. Experimental (dots) and modelled (lines) PL dynamics using equations S11, S12 and S13, for the perovskite film with (a) and without (b) the ionic additives. Initial distribution of charge-carriers was considered to be uniform across the film thickness in this case. Data and model were normalized at t=20 ns to better visualise the dynamics without the early-time components associated with surface and diffusion effects.

Figure S5 shows that the PL dynamics of the perovskite films fabricated with the ionic additive can be very accurately described by equal decay rates for electrons and holes, while the fluence dependence observed for the control sample can be reproduced by unbalanced rates. We note that although we present k_{tp} to be higher than k_{tn}, these two parameters are interchangeable and the opposite rates result in equal PL dynamics.

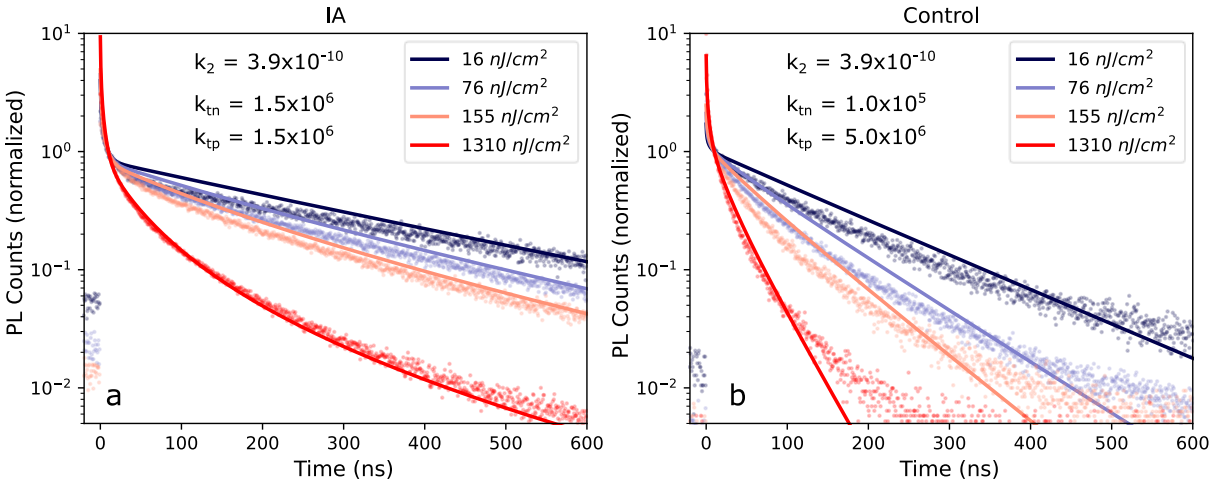

Figure S6. Experimental (dots) and modelled (lines) PL dynamics using equations S11, S12 and S13, for the perovskite film with (a) and without (b) the ionic additives. Initial distribution of charge-carriers was calculated from the absorption coefficients (see **Figure S1**) at the pump wavelength (400 nm), and diffusion effects have been simulated up to 20 ns (after uniform distribution has been reached). Data and model were normalized at t=10 ns to better visualise the comparison of dynamics.

To better account for the early-time recombination, we have then implemented the simulation of diffusion effects. For such, we first calculate the photogeneration profile across 100 slices of the film thickness, resulting from the absorption of the 400 nm light (according to the absorption coefficients shown in **Figure S1**). Diffusion is calculated using a forward Euler method similar to previous reports.[20] The limited temporal resolution of the TCSPC experiment for acquiring the PL dynamics does not allow for a precise analysis of the early-time components of the decay. However, any significant differences in the diffusion dynamics would have an impact on the recombination observed in the OPTP experiment. As no differences had been observed, the diffusion coefficients were kept fixed for both films with and without ionic additives.

Figure S6 shows the PL dynamics modelled with implemented diffusion effects, using the same recombination rate constants obtained previously when considering uniform distribution of charge-carriers as the initial photoexcitation conditions (**Figure S5**). We note that other effects could play a role in the stretching of the decays, such as variations in the ambipolar diffusion upon trap state filling, lateral diffusion, photon reabsorption and the efficiency of PL outcoupling and collection. Nonetheless, we observe a very good agreement between the model and the fluence-dependence of the experimentally acquired PL dynamics. Importantly, such an agreement is reached without changes to the bimolecular radiative rate, and the difference between the control and ionic additive films result from the unbalanced electron-hole trapping dynamics, and the build-up of populations upon 1MHz repetition rate of the photoexcitation. To better understand this effect, we show in **Figure S7** the individual electron and hole lifetimes obtained from equations S11 and S12 for the case of balanced and unbalanced rates (k_{tn} and k_{tp}). When one type of carrier (electrons/holes) decays with a higher rate, the remaining population of the opposite carrier cannot recombine radiatively. If the non-radiative decay of these remaining carriers is slow enough, a significant population of free carriers will be present when the next photoexcitation pulse arrives.

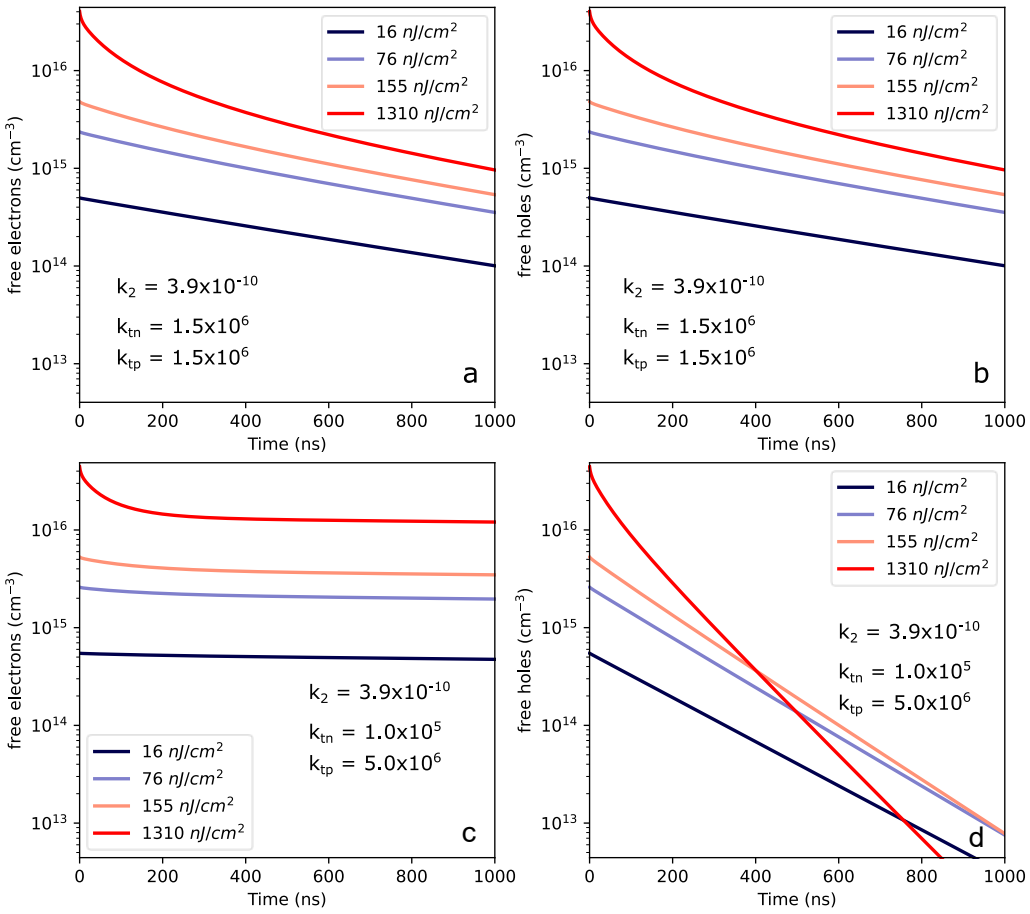

Figure S7. Electron and hole lifetimes obtained from equations S11 and S12, according to the rates used for modelling the PL dynamics of the perovskite film with ionic additives (a and b, with balanced k_{tn} and k_{tp}), and without additives (c and d, with unbalanced rates)

A sequence of pulses will then create a steady-state population that will affect the observed radiative recombination. This *photodoping* effect will depend on the photoexcitation intensity and can therefore explain the shortening of lifetimes observed with increasing fluence in the control perovskite film, even though the bimolecular radiative rates are unchanged. **Figure S8** shows the population build-up over a sequence of 50 pulses of 1MHz photoexcitation. For comparison, we can also observe in **Figure S8c,d** that 5kHz photoexcitation (as used in the OPTP experiment) results in a population build-up several orders of magnitude lower, which would result in negligible effects on the recorded recombination dynamics.

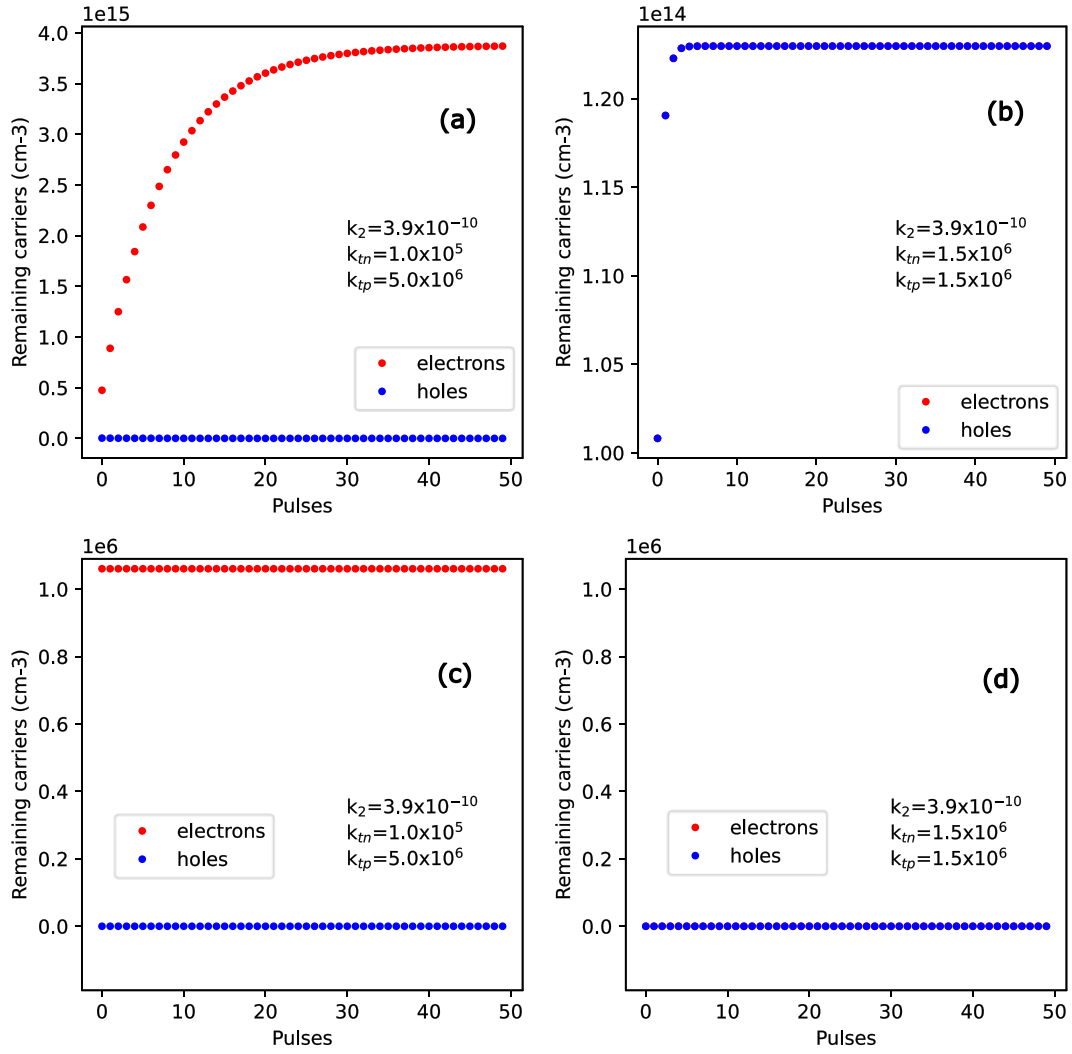

Figure S8. Remaining electron and hole populations at the time of arrival of the next pulse obtained from the **Equations S11 and S12**, at fluence 16 nJ/cm^2 with 1MHz (a,b) and 5kHz (c,d) repetition rate, for balanced (b,d) and unbalanced (a,c) electron and hole rate constants k_{tn} and k_{tp}.

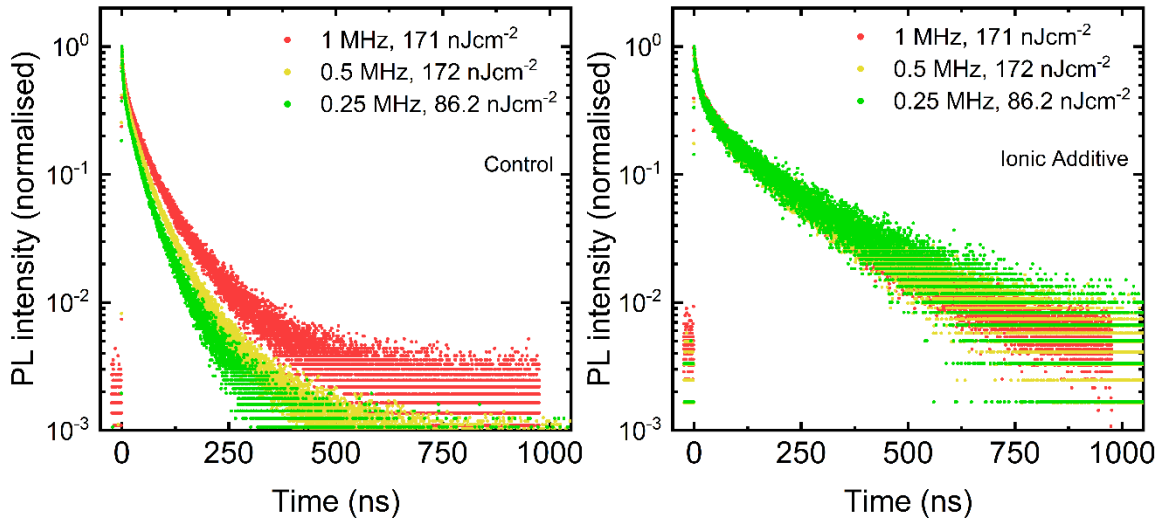

Figure S9: Time-correlated single photon counting measurements for control (left panel) and IA modified (right panel) perovskite think films on quartz. The films were excited using a 398 nm centre wavelength laser at a range of repetition rates, 1 MHz (red), 500 kHz (yellow) and 250 kHz (green). The fluences were kept as constant as possible between each fluence. Importantly, the lifetimes are shorter for less frequent excitation pulses in the control sample, whereas the lifetimes are repetition rate independent for the IA modified sample. This supports the assumption of trap-filling and population build-up being substantial in the control sample, and less significant in the IA modified perovskite thin film.

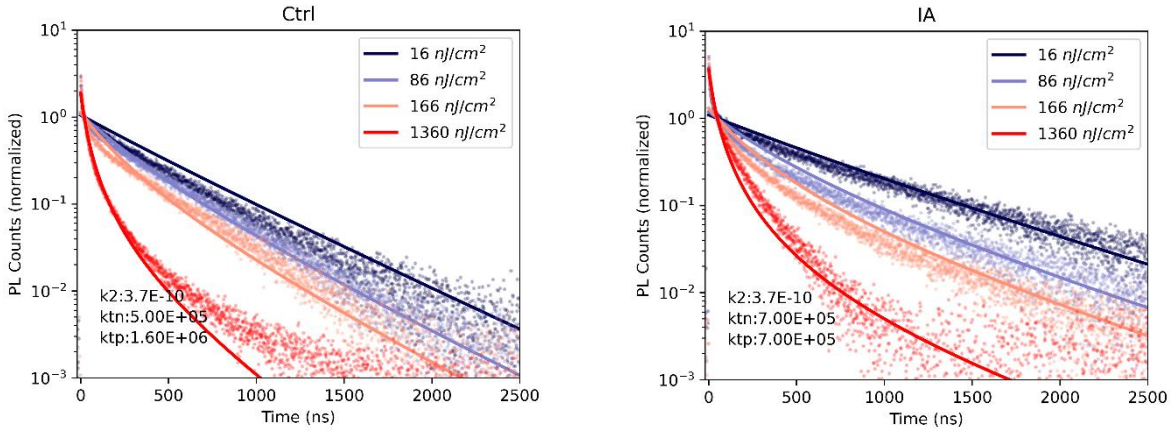

Figure S10: Time-correlated single photon counting (TCSPC) transients for control (left) and IA modified (right) perovskite thin film samples. The samples were illuminated from the quartz side with a 398 nm centre wavelength laser with a 250 kHz repetition rate at a range of fluences. The dark lines are the fits to the PL transients calculated using unbalanced first-order recombination rates for the control, and balanced rates for the IA sample.

Interface recombination

Fluence-dependent TCSPC on partial device stacks

For each partial device stack, we performed time-correlated single photon counting (TCSPC) studies with excitation fluences of 16, 76, 155 and 1310 nJcm^{-2}. It is well known that the lifetimes of isolated (no transport layers) perovskite thin-films on glass decrease with monotonically with increasing fluence[24], which agrees with our results in **Figures 1c&1d** in the main text. For the partial device stacks, in addition to non-radiative recombination in the perovskite bulk, charge transfer into the CTL as well as interfacial recombination becomes important.[24,25] Further, charge accumulation may play a non-negligible role, especially at higher fluences. Charge transfer happens on shorter time scales, resulting in an initial fast drop in the PL intensity.[25] Therefore at each fluence, we see an initially low differential lifetime (due to the rapid charge transfer), which then increases at longer delay times. This plateau is the effective interface recombination lifetime, which we use to determine the SRV.

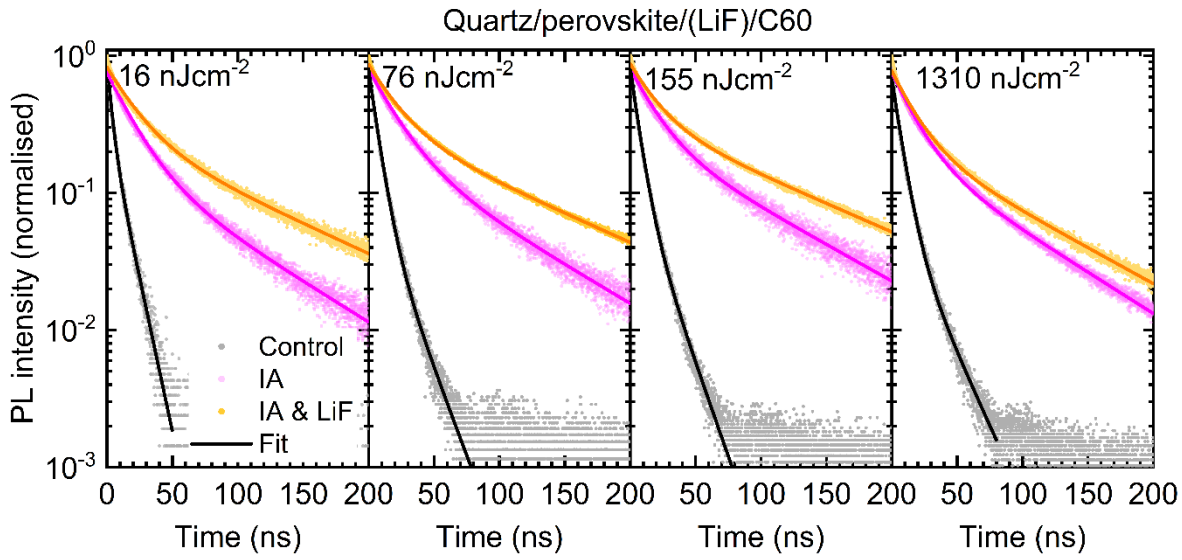

Figure S11: Photoluminescence transients measured using time-correlated single photon counting, with a pulsed laser of centre wavelength 398 nm and repetition rate of 2.5 MHz. The samples were quartz/perovskite/(LiF)/C60 and were illuminated from the quartz side to avoid parasitic absorption in the transport layer. The excitation fluences ranged from 16 nJcm^{-2} (left panel) to 1310 nJcm^{-2} (right panel).

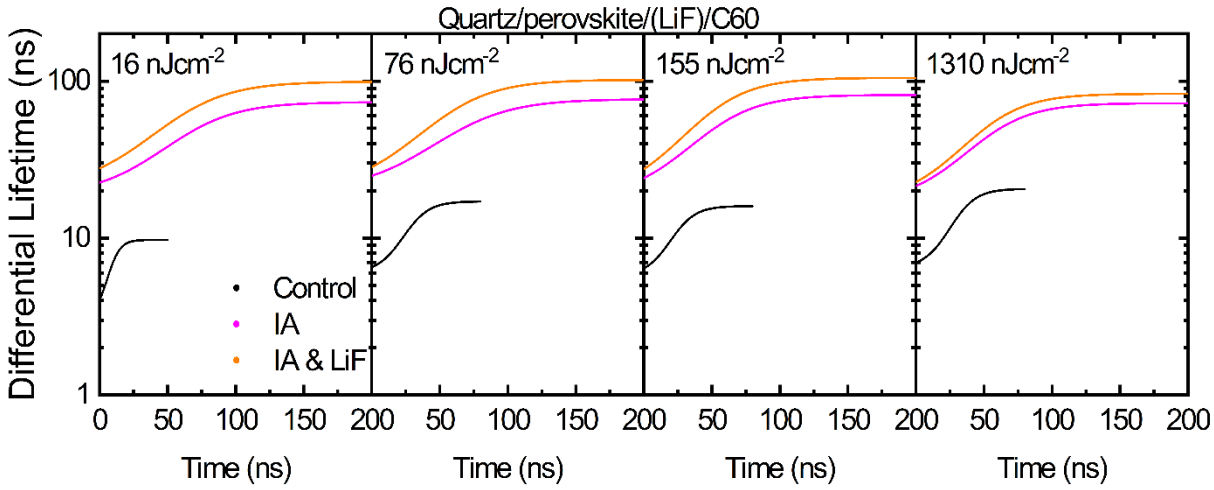

Figure S12: Differential lifetimes determined from **equation 1** in the main text from the double exponential fits to the PL transients presented in **figure S9**. The samples were quartz/perovskite/(LiF)/C60 and were illuminated from the quartz side to avoid parasitic absorption in the transport layer. The excitation fluences ranged from 16 nJcm^{-2} (left panel) to 1310 nJcm^{-2} (right panel).

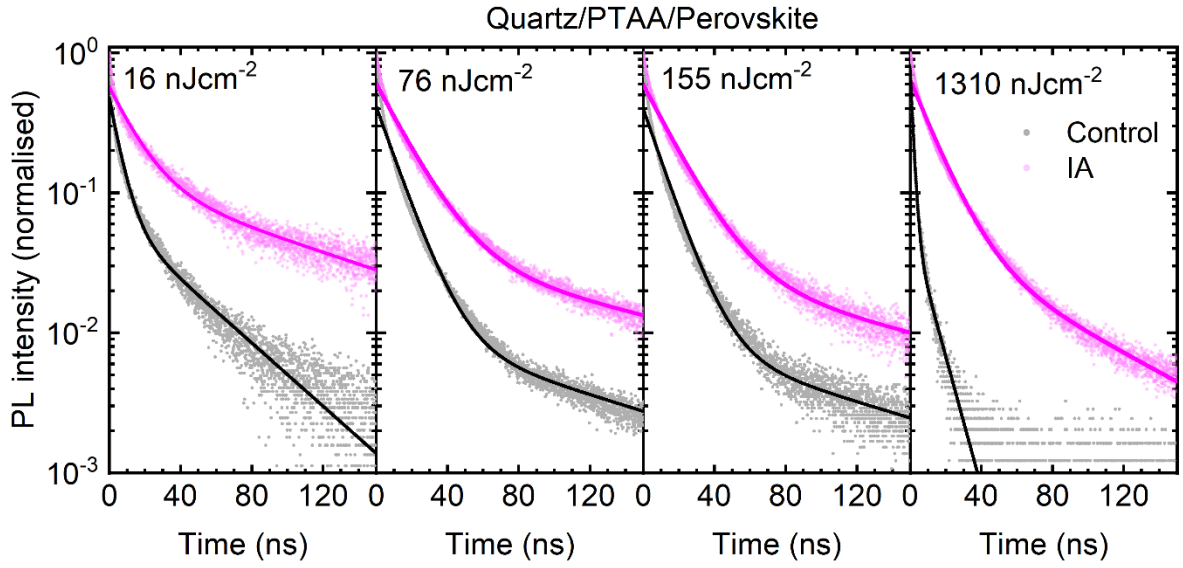

Figure S13: Photoluminescence transients measured using time-correlated single photon counting, with a pulsed laser of centre wavelength 398 nm and repetition rate of 2.5 MHz. The samples were

quartz/PTAA/perovskite and were illuminated from the perovskite side. The excitation fluences ranged from 16 nJcm^{-2} (left panel) to 1310 nJcm^{-2} (right panel).

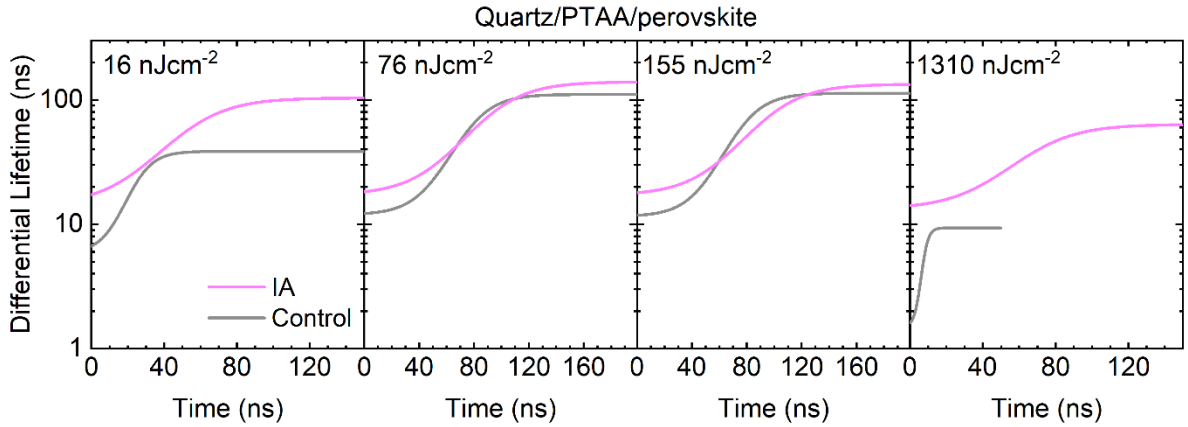

Figure S14: Differential lifetimes determined from **equation 1** in the main text from the double exponential fits to the PL transients presented in **figure S11**. The samples were quartz/PTAA/perovskite and were illuminated from the perovskite side. The excitation fluences ranged from 16 nJcm^{-2} (left panel) to 1310 nJcm^{-2} (right panel).

Justification of double exponential fit

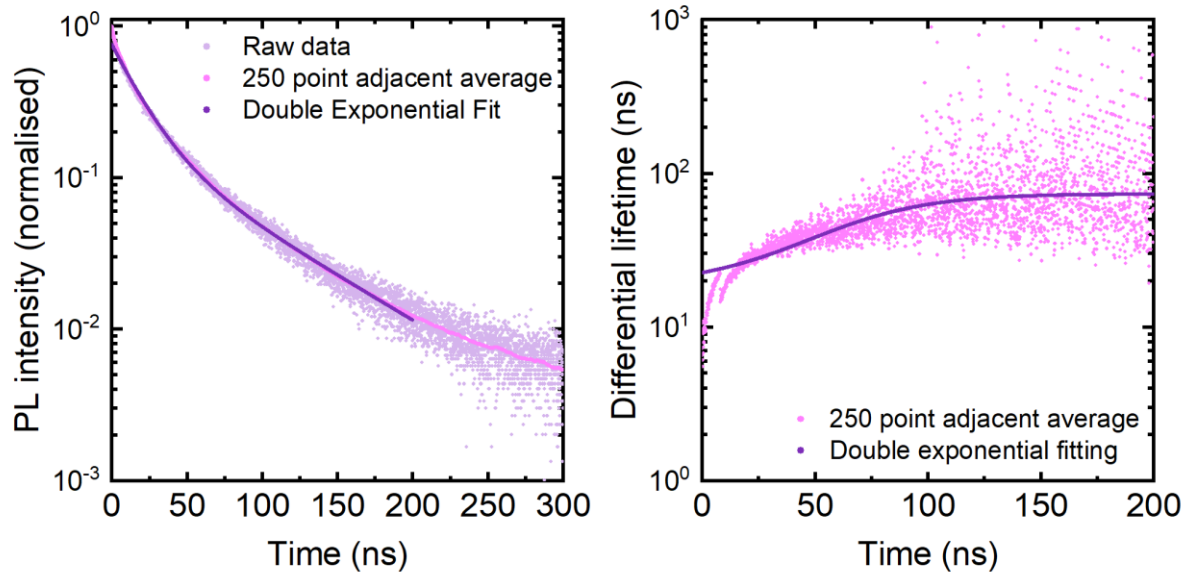

Figure S15: Justification of the double exponential fit. The left panel displays the PL transient (light purple) shown in **Figure 2d** in the main text for the quartz/IA modified perovskite/C60 sample, illuminated from the quartz side with a fluence of 16 nJcm^{-2}. We display the same double exponential fit (dark purple) from the main text and compare this fit with the smoothed data (pink).

A 250 point adjacent average was chosen as this was the largest window that didn't create significant artefacts in the differential lifetime. As can be seen in the left panel, the double exponential fit accurately reproduces the data and lies close to the smoothed data, demonstrating the validity of this approach. The right panel shows the differential lifetime calculated from **equation 1** from the main text, using the smoothed data (pink) and double exponential fit (dark purple). The discontinuity in the differential lifetime from the smoothed data at 16 ns comes from the finite size of the smoothing window (64 ps bin size* 250 point window = 16 ns). As can be seen from the figure, the fit using the double exponential is significantly less noisy, yet lies at the "centre of mass" of the smoothed data demonstrating the validity of this approach.

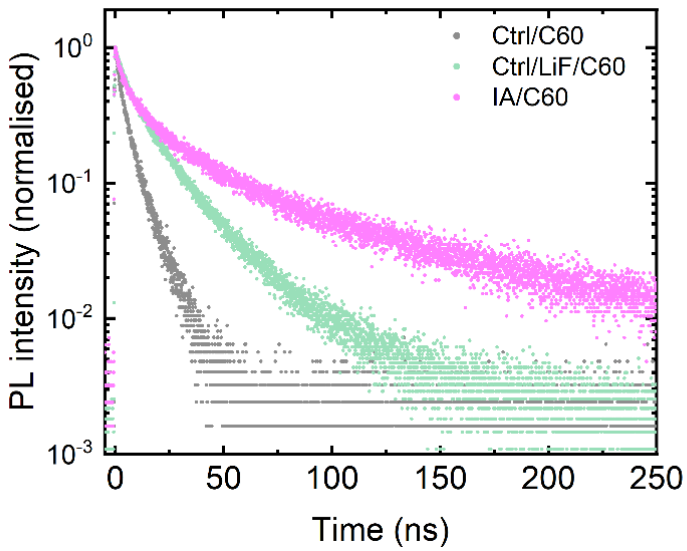

Figure S16: Time-correlated single photon counting (TCSPC) transients for quartz/perovskite/C60 samples with control perovskite (grey symbols), control perovskite with a LiF interlayer (green symbols) and IA modified (pink symbols) perovskite. The samples were illuminated from the quartz side with a 398 nm centre wavelength laser at a fluence of 31 nJcm^{-2}.

Photovoltaic device performance

Investigation of short-circuit current density increase

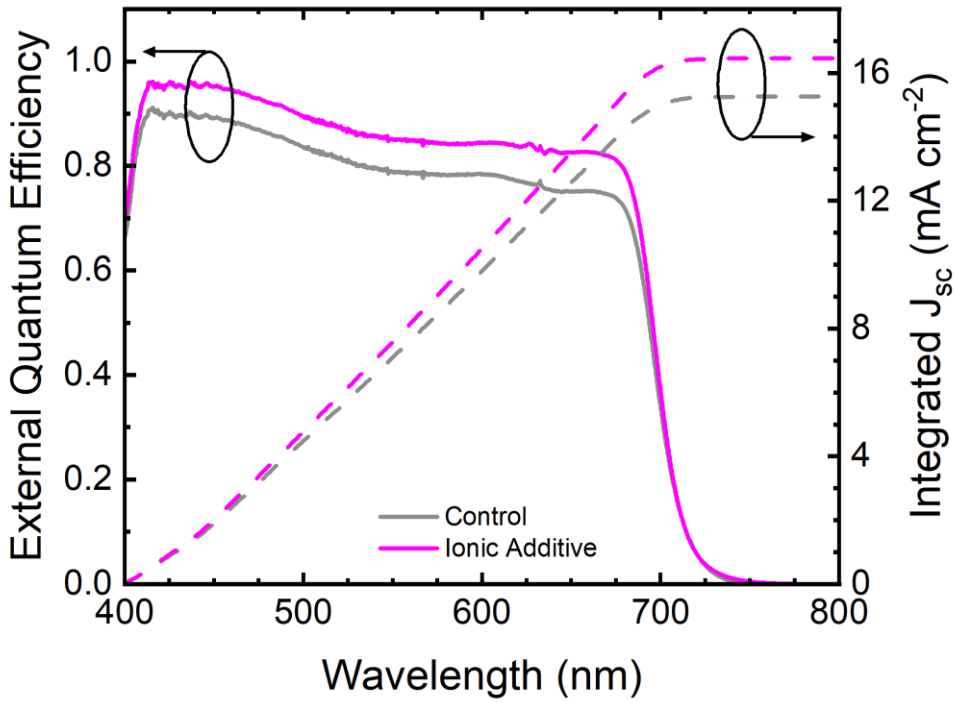

Figure S17: External quantum efficiency and integrated short-circuit current density for representative control (grey) and IA modified (purple) devices. The integrated current shows good agreement with the J_{sc} determined from the JV curves. Explicitly, the J_{sc} determined from the *JV* curves was 15.0 mAcm^{-2} and 16.8 mAcm^{-2} which compares to 15.2 mAcm^{-2} and 16.5 mAcm^{-2} integrated current densities for control and IA modified devices respectively.

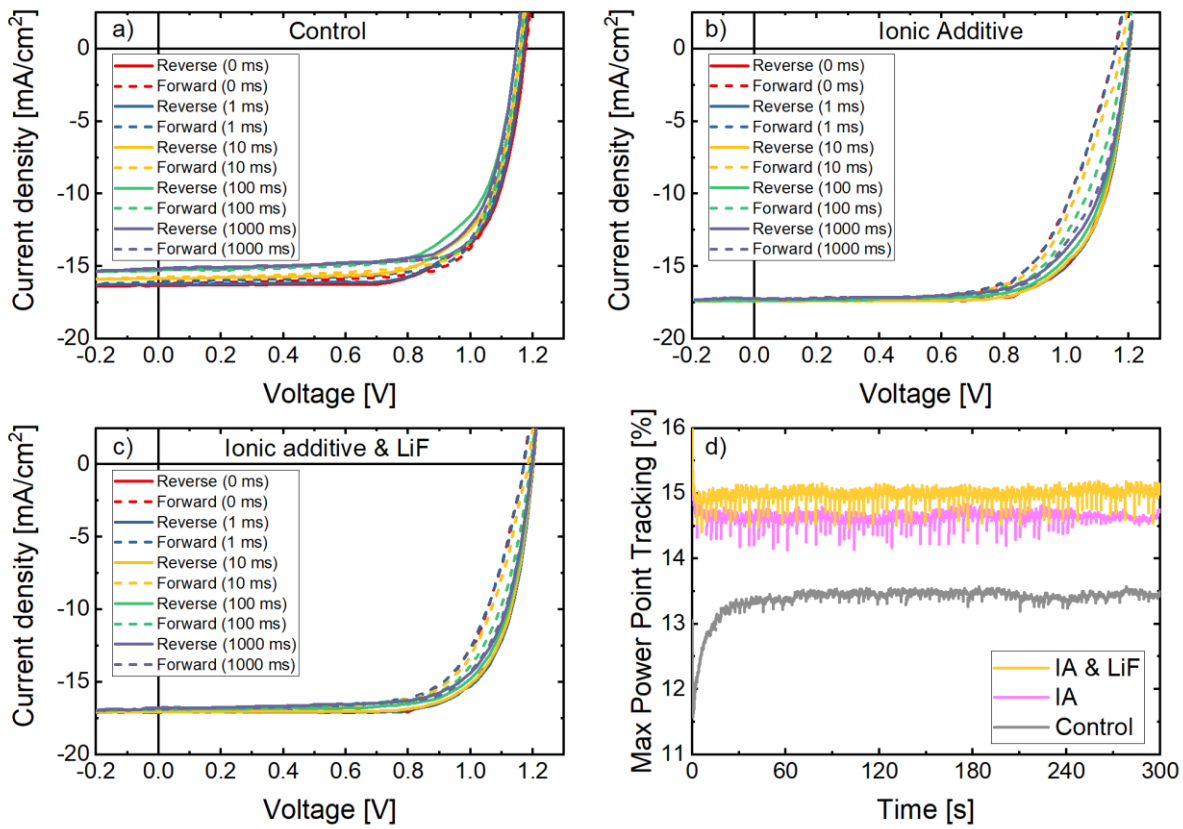

Figure S18: Forward and reverse scans at a wide range of settling times (0-1000 ms) for representative a) control, b) IA modified and c) IA modified with a LiF interlayer devices. d) Maximum power point tracking for the same devices recorded over 5 minutes.

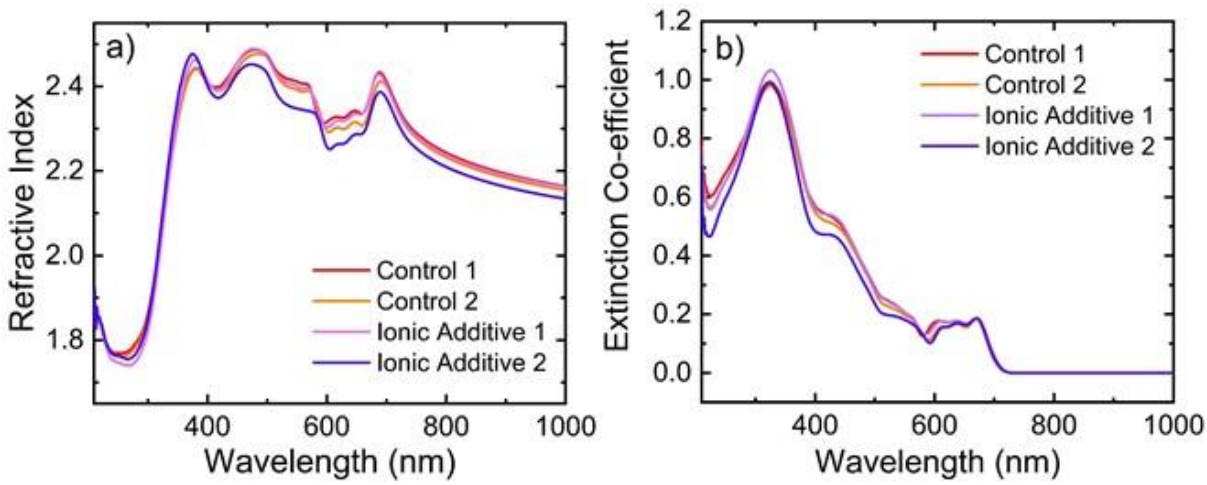

Figure S19*:* a) refractive index and b) extinction coefficient of the neat (Control 1, red & Control 2, orange) and treated (Ionic Additive 1, light purple & Ionic Additive 2, dark purple) thin films deposited on z-cut quartz substrates as determined by ellipsometry. All samples have similar optical constants, and so the increased J_{sc} is unlikely to be due increased charge carrier generation following IA incorporation.

Recombination studies in devices

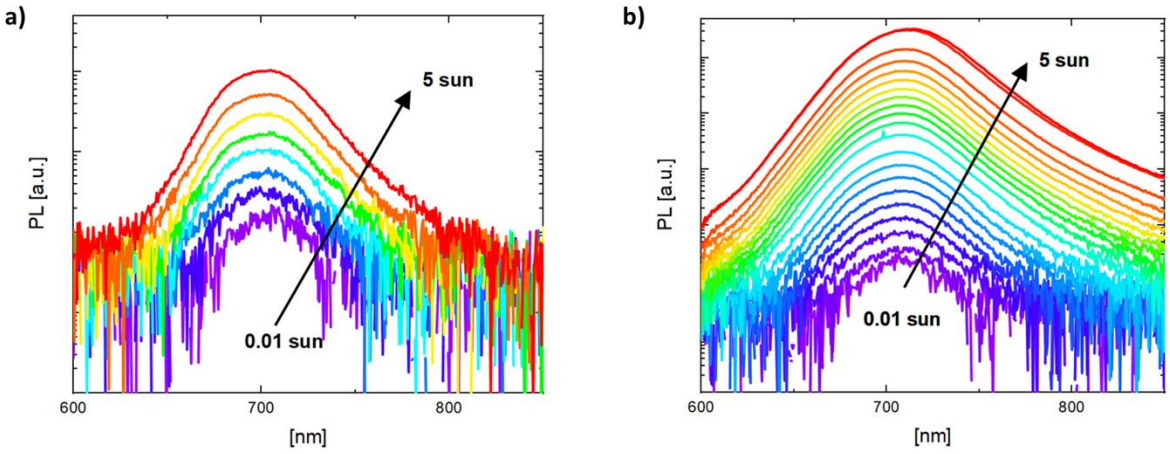

Figure S20: Intensity dependent PL spectra for a control a) and IA modified b) perovskite thin films on glass. In both cases we observe not shift in the PL peak under constant illumination and high illumination intensities indicating absence of phase segregation.

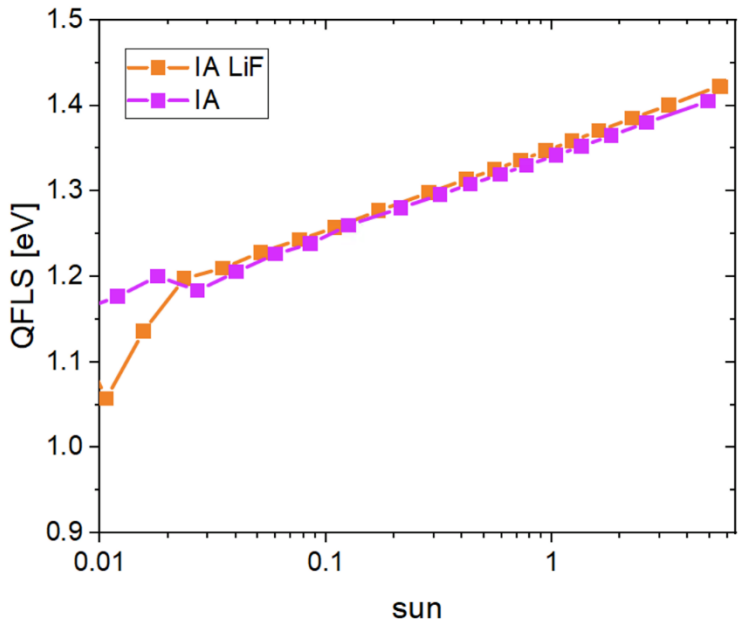

Figure S21: Intensity dependent QFLS measurements for IA additive modified perovskite thin films on glass. The sample corresponding to the data shown in orange had a ~1 nm LiF layer deposited on top of the perovskite. As can be seen in the figure, the presence of this LiF layer does not affect the absolute value of the QFLS, nor the ideality factor, which explains the similarity of the *pJV* curves, determined from QFLS(*I*) measurements, in Table 2 in the main text.

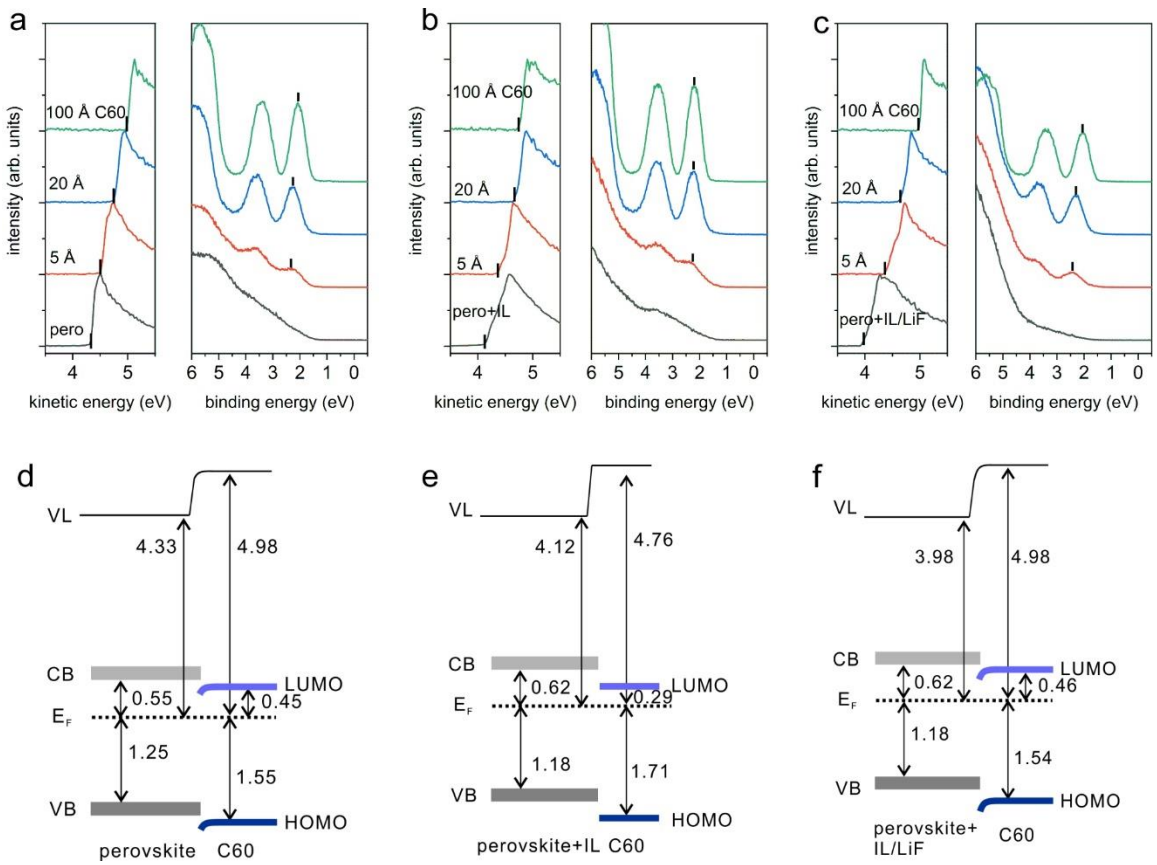

Figure S22: Ultraviolet photoemission spectroscopy (UPS) measurements. a), b) and c) show the UPS measurements for control, IA-modified and IA-modified & LiF perovskite thin films on ITO/PTAA substrates respectively. Sequential deposition of C60 was performed and UPS measurements were repeated at C60 thicknesses of 5, 20 and 100 Å, allowing the reconstruction of the energetics at this interface. In a), b) and c), the left panel shows the secondary electron cut-off which gives the work function, and the right panel shows the valance band region, from which the valence band onset is extracted. d), e) and f) show the flat-band diagrams of this interface using the measurements from a), b) and c) respectively.

We find that the control perovskite exhibits an initially strong n-type surface with the valence band (VB) onset of 1.25 eV (extrapolated on a logarithmic intensity scale as commonly applied for perovskites) with respect to Fermi level (E_F) set at 0.[26,27] The strong n-type character is slightly suppressed upon IA addition with the VB onset positioned at 1.18 eV. This could be ascribed to the reduction of the surface defect density which shifts the E_F towards mid-gap, in agreement with the increased PLQY observation upon IA addition. In addition, the perovskite/C60 interfaces present a type-II heterojunction for all cases in favour of charge transport across the interface. However, the energy offset between the conduction band of the FACs IA and the lowest unoccupied molecular

orbital of the C60 appears to be slightly increased as compared to other two cases, despite the observed increase of the device V_{OC} employing IA.

Drift-diffusion simulations

As discussed in earlier, the drift-diffusion measurements were performed using SCAPS, and the input parameters can be found above.

Table S3: Comparing the device performance parameters of actual devices without (control) and with IA modification (IA) with those determined using drift-diffusion simulations, taking the mobility, bulk lifetimes and SRVs values that were determined in the main text. A full list of the device simulation inputs can be found in **Table S2**.

Condition	J_{sc} (mAcm^{-2})	FF (%)	Voc (V)	PCE (%)
Control	17.0 ± 0.5	68±2	1.16 ± 0.01	13.7 ± 0.5
Control Simulated	16.8	70.0	1.18	14.0
IA	17.5 ± 0.5	72 ± 3	1.20 ± 0.01	15.2 ± 0.5
IA Simulated	16.9	75.9	1.21	15.6

As can be seen from **Table S3,** we accurately reproduce the real photovoltaic device performance with the drift-diffusion simulations which, as far as possible, took experimentally determined values as their input. We note that we slightly overestimate the fill factor and open-circuit voltage in each case. This could be due to a number of factors, however the trend is reproduced with high accuracy, demonstrating the validity of our analysis.

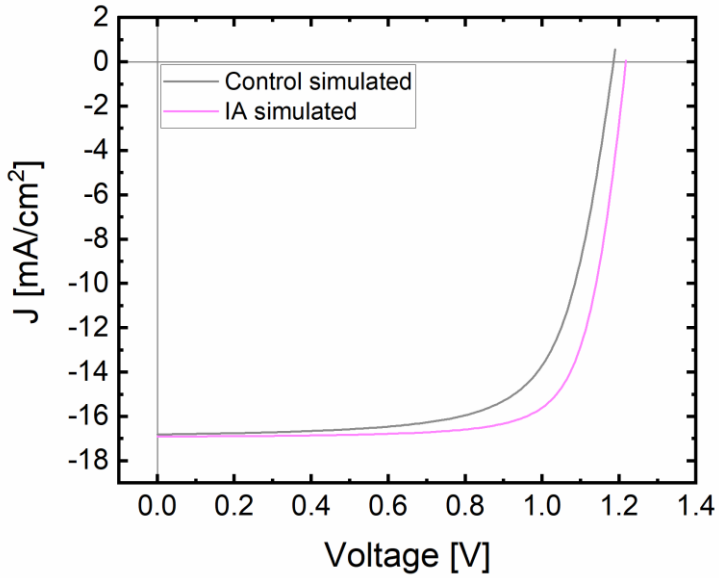

Figure S23: Comparison between the simulated *JV* curves for control (grey) and IA modified (pink) devices. The close agreement of these simulated *JV* curves with the ones measured ones demonstrates the validity of our analysis.

Supporting references

1 P. Caprioglio, M. Stolterfoht, C. M. Wolff, T. Unold, B. Rech, S. Albrecht and D. Neher, *Adv. Energy Mater.*, 2019, **9**, 1901631.

2 M. Stolterfoht, M. Grischek, P. Caprioglio, C. M. Wolff, E. Gutierrez-Partida, F. Peña-Camargo, D. Rothhardt, S. Zhang, M. Raoufi, J. Wolansky, M. Abdi-Jalebi, S. D. Stranks, S. Albrecht, T. Kirchartz and D. Neher, *Adv. Mater.*, , DOI:10.1002/adma.202000080.

3 M. Stolterfoht, P. Caprioglio, C. M. Wolff, J. A. Márquez, J. Nordmann, S. Zhang, D. Rothhardt, U. Hörmann, Y. Amir, A. Redinger, L. Kegelmann, F. Zu, S. Albrecht, N. Koch, T. Kirchartz, M. Saliba, T. Unold and D. Neher, *Energy Environ. Sci.*, 2019, **12**, 2778–2788.

4 M. Stolterfoht, C. M. Wolff, J. A. Márquez, S. Zhang, C. J. Hages, D. Rothhardt, S. Albrecht, P. L. Burn, P. Meredith, T. Unold and D. Neher, *Nat. Energy*, 2018, **3**, 847–854.

5 D. C. Johnston, *Phys. Rev. B*, 2006, **74**, 184430.

6 J. M. Richter, M. Abdi-Jalebi, A. Sadhanala, M. Tabachnyk, J. P. H. Rivett, L. M. Pazos-Outón, K. C. Gödel, M. Price, F. Deschler and R. H. Friend, *Nat. Commun.*, , DOI:10.1038/ncomms13941.

7 T. Seifert, S. Jaiswal, U. Martens, J. Hannegan, L. Braun, P. Maldonado, F. Freimuth, A. Kronenberg, J. Henrizi, I. Radu, E. Beaurepaire, Y. Mokrousov, P. M. Oppeneer, M. Jourdan, G. Jakob, D. Turchinovich, L. M. Hayden, M. Wolf, M. Münzenberg, M. Kläui and T. Kampfrath, *Nat. Photonics*, 2016, **10**, 483–488.

8 C. Wehrenfennig, M. Liu, H. J. Snaith, M. B. Johnston and L. M. Herz, *Energy Environ. Sci.*, 2014, **7**, 2269–2275.

9 M. B. Johnston and L. M. Herz, *Acc. Chem. Res.*, 2016, **49**, 146–154.

10 L. M. Herz, *Annu. Rev. Phys. Chem.*, 2016, **67**, 65–89.

11 M. Burgelman, P. Nollet and S. Degrave, *Thin Solid Films*, 2000, **361**–**362**, 527–532.

12 J. Diekmann, P. Caprioglio, M. H. Futscher, V. M. Le Corre, S. Reichert, F. Jaiser, M. Arvind, L. P. Toro, E. Gutierrez-Partida, F. Peña-Camargo, C. Deibel, B. Ehrler, T. Unold, T. Kirchartz, D. Neher and M. Stolterfoht, *Sol. RRL*, 2021, 2100219.

13 P. Caprioglio, C. M. Wolff, O. J. Sandberg, A. Armin, B. Rech, S. Albrecht, D. Neher and M. Stolterfoht, *Adv. Energy Mater.*, 2020, **10**, 2000502.

14 K. A. Bush, K. Frohna, R. Prasanna, R. E. Beal, T. Leijtens, S. A. Swifter and M. D. McGehee, *ACS Energy Lett.*, 2018, **3**, 428–435.

15 T. Leijtens, R. Prasanna, K. A. Bush, G. Eperon, J. A. Raiford, A. Gold-Parker, E. J. Wolf, S. A. Swifter, C. C. Boyd, H.-P. Wang, M. F. Toney, S. Bent and M. D. McGehee, *Sustain. Energy Fuels*, , DOI:10.1039/C8SE00314A.

16 A. F. Palmstrom, G. E. Eperon, T. Leijtens, R. Prasanna, S. N. Habisreutinger, W. Nemeth, E. A. Gaulding, S. P. Dunfield, M. Reese, S. Nanayakkara, T. Moot, J. Werner, J. Liu, B. To, S. T. Christensen, M. D. McGehee, M. F. A. M. van Hest, J. M. Luther, J. J. Berry and D. T. Moore, *Joule*, 2019, **3**, 2193–2204.

17 Z. Li, T. H. Kim, S. Y. Han, Y. J. Yun, S. Jeong, B. Jo, S. A. Ok, W. Yim, S. H. Lee, K. Kim, S. Moon, J. Y. Park, T. K. Ahn, H. Shin, J. Lee and H. J. Park, *Adv. Energy Mater.*, 2020, **10**, 1–16.

18 Y.-H. Lin, N. Sakai, P. Da, J. Wu, H. C. Sansom, A. J. Ramadan, S. Mahesh, J. Liu, R. D. J. Oliver, J. Lim, L. Aspitarte, K. Sharma, P. K. Madhu, A. B. Morales-Vilches, P. K. Nayak, S. Bai, F. Gao, C. R. M. Grovenor, M. B. Johnston, J. G. Labram, J. R. Durrant, J. M. Ball, B. Wenger, B. Stannowski and H. J. Snaith, *Science (80-.).*, 2020, **369**, 96–102.

19 Y. Wang, S. Gu, G. Liu, L. Zhang, Z. Liu, R. Lin, K. Xiao, X. Luo, J. Shi, J. Du, F. Meng, L. Li, Z. Liu and H. Tan, *Sci. China Chem.*, , DOI:10.1007/s11426-021-1059-1.

20 T. W. Crothers, R. L. Milot, J. B. Patel, E. S. Parrott, J. Schlipf, P. Müller-Buschbaum, M. B. Johnston and L. M. Herz, *Nano Lett.*, 2017, **17**, 5782–5789.

21 C. L. Davies, M. R. Filip, J. B. Patel, T. W. Crothers, C. Verdi, A. D. Wright, R. L. Milot, F. Giustino, M. B. Johnston and L. M. Herz, *Nat. Commun.*, 2018, **9**, 293.

22 S. G. Motti, D. Meggiolaro, S. Martani, R. Sorrentino, A. J. Barker, F. De Angelis and A. Petrozza, *Adv. Mater.*, 2019, **31**, 1901183.

23 A. M. Ulatowski, A. D. Wright, B. Wenger, L. R. V. Buizza, S. G. Motti, H. J. Eggimann, K. J. Savill, J. Borchert, H. J. Snaith, M. B. Johnston and L. M. Herz, *J. Phys. Chem. Lett.*, 2020, **11**, 3681–3688.

24 T. Kirchartz, J. A. Márquez, M. Stolterfoht and T. Unold, *Adv. Energy Mater.*, 2020, **10**, 1904134.

25 B. Krogmeier, F. Staub, D. Grabowski, U. Rau and T. Kirchartz, *Sustain. Energy Fuels*, 2018, **2**, 1027–1034.

26 F. Zu, P. Amsalem, D. A. Egger, R. Wang, C. M. Wolff, H. Fang, M. A. Loi, D. Neher, L. Kronik, S. Duhm and N. Koch, *J. Phys. Chem. Lett.*, 2019, **10**, 601–609.

27 J. Endres, D. A. Egger, M. Kulbak, R. A. Kerner, L. Zhao, S. H. Silver, G. Hodes, B. P. Rand, D. Cahen, L. Kronik and A. Kahn, *J. Phys. Chem. Lett.*, 2016, **7**, 2722–2729.